Lattice QCD determination of the radiative decay rates $h_c \to \eta_c\gamma$ and $h_b \to \eta_b\gamma$

D. Bečirević,[1] R. Di Palma,[2] R. Frezzotti,[3] G. Gagliardi,[2] V. Lubicz,[2] F. Sanfilippo,[4] and N. Tantalo[3]

[1]*IJCLab, Pôle Théorie (Bat. 210), CNRS/IN2P3 et Université, Paris-Saclay, 91405 Orsay, France*
[2]*Dipartimento di Matematica e Fisica, Università Roma Tre and INFN, Sezione di Roma Tre, Via della Vasca Navale 84, I-00146 Rome, Italy*
[3]*Dipartimento di Fisica and INFN, Università di Roma "Tor Vergata", Via della Ricerca Scientifica 1, I-00133 Roma, Italy*
[4]*Istituto Nazionale di Fisica Nucleare, Sezione di Roma Tre, Via della Vasca Navale 84, I-00146 Rome, Italy*

(Received 12 May 2025; accepted 31 July 2025; published 19 August 2025)

We present the results of our lattice QCD computation of the hadronic matrix elements relevant to the $h_c \to \eta_c\gamma$ and $h_b \to \eta_b\gamma$ decays by using the gauge configurations produced by the Extended Twisted Mass Collaboration with $N_f = 2+1+1$ dynamical Wilson-Clover twisted mass fermions at five different lattice spacings with physical dynamical u, d, s and c quark masses (except for the coarsest lattice for which the lightest sea quark corresponds to a pion with $m_\pi \simeq 175$ MeV). While the hadronic matrix element for $h_c \to \eta_c\gamma$ is obtained directly, the one relevant to $h_b \to \eta_b\gamma$ is reached by working with heavy quark masses $m_H^{(n)} = \lambda^{n-1} m_c$, with $\lambda \sim 1.24$ and $n = 1, 2, \ldots, 6$, and then extrapolated to m_b by several judicious *Ansätze*. In the continuum limit we obtain $\Gamma(h_c \to \eta_c\gamma) = 0.604(24)$ MeV, which is by a factor of 2.3 more accurate than the previous lattice estimates, and in good agreement with the experimental measurement. In the b-quark case we obtain $\Gamma(h_b \to \eta_b\gamma) = 46.0(4.8)$ keV.

DOI: 10.1103/ysxn-sxj7

I. INTRODUCTION

In recent years, the radiative decays of heavy quarkonia have attracted considerable interest, particularly with the experimental detection of the η_b meson by *BABAR* [1]. The study of the so-called electric dipole (E1) and magnetic dipole (M1) transitions, such as $h_{c(b)} \to \eta_{c(b)}\gamma$, $J/\Psi \to \eta_c\gamma$ and $\Upsilon(nS) \to \eta_b\gamma$, can give further insight in the internal structure and dynamics of heavy quarkonium states conveniently described by a suitable effective field theory [2–5].

The experimental challenge in measuring decay processes with limited phase space, such as $\Upsilon(1S) \to \eta_b\gamma$, has led experimenters to focus on decays of the radially excited states, such as $\Upsilon(2S) \to \eta_b\gamma$ and $\Upsilon(3S) \to \eta_b\gamma$ [1,6–8]. These studies helped in extracting m_{η_b} and provided us with estimates of the hyperfine splitting, the value of which has been recently updated to $\Delta_b^{\rm exp} = m_{\Upsilon(1S)} - m_{\eta_b} = 62.3 \pm 3.2$ MeV [9], after the reassessment of uncertainties in the old extractions of $m_{\Upsilon(1S)}$ [10]. Note that its value is about 2σ larger than predicted by a resummation of perturbative QCD series in Refs. [11,12]. Lattice QCD provides a way to compute that quantity model independently. While the initial lattice results pointed to a small value for $\Delta_b^{\rm latt} \lesssim 40$ MeV [13,14], it subsequently became clear that working with much lighter sea quark masses lead to larger values for hyperfine splitting. Indeed, in the studies with $N_f = 2+1$ staggered light quarks and with the so-called Fermilab approach to heavy quarks [15], $\Delta_b^{\rm latt} = 54 \pm 12$ MeV was reported in Ref. [16]. Instead, by using the nonrelativistic QCD (NRQCD) treatment of a heavy quark on the lattice, the values $\Delta_b^{\rm latt} \approx 60 \pm 8$ MeV and $\Delta_b^{\rm latt} \approx 70 \pm 9$ MeV have been obtained in [17,18], respectively, thus consistent with $\Delta_b^{\rm exp}$.

Another recent experimental effort carried out by Belle focused on $\Upsilon(4S) \to h_b(1P)\gamma$ followed by $h_b(1P) \to \eta_b\gamma$ [19]. That measurement yields $\Delta_b^{\rm exp}$ fully consistent with the value quoted above, and it allowed the authors to extract $\mathcal{B}(h_b \to \eta_b\gamma) = (56 \pm 8 \pm 4)\%$, improving on their previous Ref. [20]. Besides the importance of confronting the theory with the experiment, Δ_b and $\mathcal{B}(h_b \to \eta_b\gamma)$ are important for searches of physics beyond the Standard Model (BSM). For example, in the models in which the Higgs sector is extended by one or more Higgs doublets, one can check whether or not a CP-odd Higgs state (A) is light because in that case it can mix with a quarkonium with

Published by the American Physical Society under the terms of the Creative Commons Attribution 4.0 International license. Further distribution of this work must maintain attribution to the author(s) and the published article's title, journal citation, and DOI. Funded by SCOAP³.

the same quantum number, such as η_c or η_b. Mixing with η_b has been abundantly studied in Refs. [21–24]. Another BSM possibility is that of an axionlike particle a (ALP), which arises in scenarios in which the mass (m_a) and the coupling (f_a) are independent and not related as $f_a m_a \approx f_\pi m_\pi$, like in the usual QCD axion. ALP can therefore be heavy and, being a pseudoscalar, it can mix with η_c or η_b, and alter the experimentally observed decay modes involving the pseudoscalar states identified as η_c or η_b [25–28]. For that reason, it is very important to have a precise QCD based determination of the hyperfine splitting and of the relevant transition matrix elements. In this paper we focus on the latter.

Previous works in lattice QCD have shown that the radiative decays of charmonia, such as $J/\psi \to \eta_c\gamma$ and $h_c \to \eta_c\gamma$, can be computed with a satisfactory precision [29], allowing for a systematic extrapolations to the continuum limit with a corresponding uncertainty under control [30–32]. Following the methodology of Ref. [30], the present study seeks to improve upon these calculations by focusing on the electric dipole (E1) transition of charmonia, $h_c \to \eta_c\gamma$, which is then extended to the case of bottomonia, $h_b \to \eta_b\gamma$, which is a new lattice result. For this calculation we employ five different fine lattice spacings in the range $a \in [0.049\text{–}0.09]$ fm.

In contrast to the charmonium system, which can be directly simulated on current lattices, the bottomonium one is computationally challenging because the ultraviolet (UV) cutoff scale employed in current simulations ($\propto 1/a$, the inverse lattice spacing) is smaller than the b-quark mass (m_b). To circumvent this problem, we use a sequence of heavy quark masses lighter than the physical b-quark, $m_H < m_b$, however larger than the physical m_c. In selecting the heavy quark masses we choose $am_H \lesssim 0.5$, as to keep the ultraviolet (UV) cutoff effects under control. In this respect, particularly beneficial are the two ensembles of gauge field configurations, produced by the Extended Twisted Mass Collaboration (ETMC), with lattice spacings $a \approx 0.058$ fm and $a \approx 0.049$ fm, which allow us to reach the heavy quarks up to nearly three times the charm quark mass. To obtain the results at the physical point (corresponding to $m_H \to m_b$), we guided our extrapolation by phenomenological parametrizations inspired by NRQCD.

The remainder of this paper is organized as follows. In Sec. II, we discuss the charmonium decay $h_c \to \eta_c\gamma$, where we work directly at the physical charm quark mass for which we provide a precise estimate of the relevant form factor and therefore the decay width. In Sec. III, we focus on the bottomonium decay $h_b \to \eta_b\gamma$. We employ the ratio method of Ref. [33] to reduce systematic errors, enhance statistical precision, and suppress lattice discretization effects in the determination of the radiative heavyonium decay width for $m_c < m_H < m_b$. We then present the results of the continuum limit extrapolation for each of the simulated heavy quark masses, discuss the various scaling relations used to extrapolate to the physical b-quark mass, and present our final results for the nonperturbative transition form factor describing $h_b \to \eta_b\gamma$. Finally, in Sec. IV, we compare our results to experimental measurements and/or existing theoretical calculations, and in Sec. V we summarize the implications of our results outlining potential directions for future research.

II. LATTICE SETUP AND CALCULATION OF THE $h_c \to \eta_c\gamma$ TRANSITION FORM FACTOR

The transition matrix element describing the radiative decay $h_c \to \eta_c\gamma$ is given by [29],

$$\begin{aligned}&\langle \eta_c(k)|J^\mu_{\rm em}|h_c(p,\varepsilon_\lambda)\rangle \\ &= 2iQ_c\left\{ m_{h_c}F_1^c(q^2)\left(\varepsilon^{*\mu}_\lambda - \frac{\varepsilon^*_\lambda\cdot q}{q^2}q^\mu\right)\right. \\ &\quad \left. + F_2^c(q^2)(\varepsilon^*_\lambda\cdot q)\left[\frac{m^2_{h_c}-m^2_{\eta_c}}{q^2}q^\mu - (p+k)^\mu\right]\right\}, \end{aligned} \tag{1}$$

where $J^\mu_{\rm em}$ is the electromagnetic current,

$$J^\mu_{\rm em}(x) = \sum_{f=u,d,s,c} J^\mu_f(x) = \sum_{f=u,d,s,c} Q_f \bar{q}_f(x)\gamma^\mu q_f(x), \tag{2}$$

and the sum runs over all quark flavors $f = \{u,d,s,c\}$, $q_f(x)$ is the quark field, and Q_f the quark electric charge in units of the elementary charge e. In Eq. (1), p and k are the momenta of the h_c and η_c mesons, respectively, and $q = p - k$, while ε_λ is the polarization vector of the h_c. The form factors at $q^2 = 0$ satisfy the relation $m_{h_c}F_1^c(0) = (m^2_{h_c} - m^2_{\eta_c})F_2^c(0)$, and therefore the corresponding rate of the decay to a real photon can be expressed in terms of the single transition form factor $F_1^c \equiv F_1^c(0)$ through,

$$\Gamma(h_c \to \eta_c\gamma) = \frac{2Q_c^2}{3}\alpha_{\rm em}\frac{m^2_{h_c}-m^2_{\eta_c}}{m_{h_c}}|F_1^c|^2, \tag{3}$$

which thus encodes all the nonperturbative information on the decay.

To compute the form factor F_1^c on the lattice, we make use of the gauge configurations produced by the ETMC with $N_f = 2+1+1$ dynamical Wilson-Clover twisted mass fermions. This framework guarantees the automatic $O(a)$ improvement of parity-even observables [34,35]. Basic information regarding the five lattice ensembles used in this work is provided in Table I, and further details can be found in Ref. [36]. In this work we employ the mixed-action lattice setup introduced in Ref. [35], and described in the appendixes of Ref. [36]. In this setup, the action of the valence quarks is discretized in the so-called Osterwalder–Seiler (OS) regularization, namely,

TABLE I. $N_f = 2+1+1$ ETMC gauge ensembles used in this calculation. We give the spatial extent in lattice units L/a, the lattice spacing a, the bare charm quark mass am_c, the renormalization constant of the vector current Z_V determined in Ref. [36] using the twisted-mass Ward identity, and the number of gauge configurations N_g. With the exception of the A48 ensemble which corresponds to a pion mass $m_\pi \simeq 175$ MeV, all the ensembles have been generated at physical values of the light, strange and charm quark masses.

ID	L/a	a fm	Z_V	am_c	N_g
A48	48	0.0907(5)	0.68700(15)	0.2620	300
B64	64	0.07948(11)	0.706354(54)	0.23157	203
C80	80	0.06819(14)	0.725440(33)	0.19840	609
D96	96	0.056850(90)	0.744132(31)	0.16490	150
E112	112	0.04892(11)	0.758238(18)	0.14125	93

$$S = \sum_{f=u,d,s,c} \sum_x \bar{q}_f(x)[\gamma_\mu \overline{\nabla}_\mu[U] - ir_f\gamma^5(W^{\rm cl}[U] + m_{\rm cr}) + m_f]q_f(x), \quad (4)$$

where $W^{\rm cl}[U]$ is the Wilson-Clover term [37], $m_{\rm cr}$ is the critical mass, m_f is the quark mass of the flavor f (with $m_u = m_d = m_l$), and $r_f = \pm 1$ is the sign of the twisted-Wilson parameter for the flavor f ($r_{u,c} = -r_{d,s} = 1$). At each lattice spacing, the charm quark mass m_c has been tuned to reproduce $m_{D_s} = 1967$ MeV.[1]

We work in the rest frame of the h_c meson ($\mathbf{p} = 0$) which means that to ensure $q^2 = 0$ one needs to give to the η_c meson a three-momentum

$$|\mathbf{k}| = \frac{m_{h_c}^2 - m_{\eta_c}^2}{2m_{h_c}} \simeq 500 \text{ MeV}. \quad (5)$$

To estimate the form factor F_1^c we consider the following three-point correlation function:

$$C_{\rm 3pt}^\mu(t_h; t_J) = \sum_{\mathbf{x},\mathbf{y},\mathbf{z}} e^{i\mathbf{k}(\mathbf{x}-\mathbf{y})} \langle 0|\mathcal{O}_{\eta_c}(\mathbf{x}, 0) J_{\rm em}^\mu(\mathbf{y}, -t_J) \times \mathcal{O}_{h_c}^\dagger(\mathbf{z}, -t_h)|0\rangle, \quad (6)$$

where $\mathcal{O}_{\eta_c}$ and $\mathcal{O}_{h_c}$ are the (Gaussian-smeared) interpolating operators of the η_c and h_c mesons,

$$\mathcal{O}_{\eta_c}(\mathbf{x}, t) = \sum_{\mathbf{y}} \bar{q}_c(\mathbf{x}, t) G_t^\eta(\mathbf{x}, \mathbf{y}) \gamma^5 q_c(\mathbf{y}, t),$$
$$\mathcal{O}_{h_c}(\mathbf{x}, t) = \sum_{\mathbf{y}} \bar{q}_c(\mathbf{x}, t) G_t^\eta(\mathbf{x}, \mathbf{y}) \sigma^{23} q_c(\mathbf{y}, t), \quad (7)$$

where $\sigma^{\mu\nu} = i[\gamma^\mu, \gamma^\nu]/2$, and

$$G_t(\mathbf{x}, \mathbf{y}) = \frac{1}{1+6\kappa}(\delta_{\mathbf{x},\mathbf{y}} + \kappa H_t(\mathbf{x}, \mathbf{y})), \quad (8)$$

with $H_t(\mathbf{x}, \mathbf{y})$ being the Gaussian smearing operator

$$H_t(\mathbf{x}, \mathbf{y}) = \sum_{\mu=1}^{3} [U_\mu^\star(\mathbf{x}, t)\delta_{\mathbf{x}+\hat{\mu},\mathbf{y}} + U_\mu^{\star\dagger}(\mathbf{x}-\hat{\mu}, t)\delta_{\mathbf{x}-\hat{\mu},\mathbf{y}}], \quad (9)$$

where $U_\mu^\star(x)$ is the so-called APE-smeared link, cf. [30]. We use the smearing parameter $\kappa = 0.4$, and fix on each ensemble the number of steps n in Eq. (7) so as to obtain a smearing radius $r_0 = a\sqrt{n}/\sqrt{\kappa^{-1}+6} \simeq 0.15$ fm, for both η_c and h_c [38]. The spatial momentum $\mathbf{k}$ is injected along the third spatial direction, i.e. $\mathbf{k} = (0, 0, |\mathbf{k}|)$. With this choice, and with the interpolating operators (7), the form factor F_1^c can be evaluated by computing only the component $C_{\rm 3pt}^1$ of the three-point correlation function (6).

The Wick contractions in Eq. (6) give rise to quark-connected and quark-disconnected contributions, cf. Fig. (1). In the following, we will refer to these contributions as *connected* and *disconnected*, respectively. The leftmost diagram corresponds to the dominant (connected) contribution, while (b), (c) and (d) correspond to the disconnected contributions. Note that the contributions corresponding to (b), (c) and (e) are expected to be very small due to the Zweig suppression.[2] Instead, diagram (d) and diagram (e) respect the SU(3) suppression in which u, d and s contributions cancel when $m_u = m_d = m_s$. In this work we focus on the evaluation of the dominant connected diagram, leaving the evaluation of the disconnected contributions for future works.[3] Clearly, only the charm quark component J_c^μ of the electromagnetic current $J_{\rm em}^\mu$ contributes to the connected part of the correlation function $C_{\rm 3pt}^\mu(t_h; t_J)$.

As far as the connected contribution is concerned, we employ the twisted boundary conditions in order to tune the spatial momentum $\mathbf{k}$ to the value of Eq. (5). This is implemented by twisting the gauge links $U_\mu(x)$ on which one of the charm quark propagators is computed, namely

$$U_\mu(x) \to U_\mu^\theta(x) = e^{ia\theta_\mu/L} U_\mu(x), \quad \theta_\mu = (0, \vec{\theta}), \quad (10)$$

with the twisting-angle $\vec{\theta}$ set to

[1]The strange quark mass has been tuned to reproduce the kaon mass value $m_K = 494.6$ MeV.

[2]The Zweig suppression is expected to be even more effective for the $h_b \to \eta_b\gamma$ decay discussed in Sec. III.

[3]A lattice QCD study of Ref. [39] shows that the contributions arising from disconnected diagrams give a tiny contribution to the masses of charmonia.

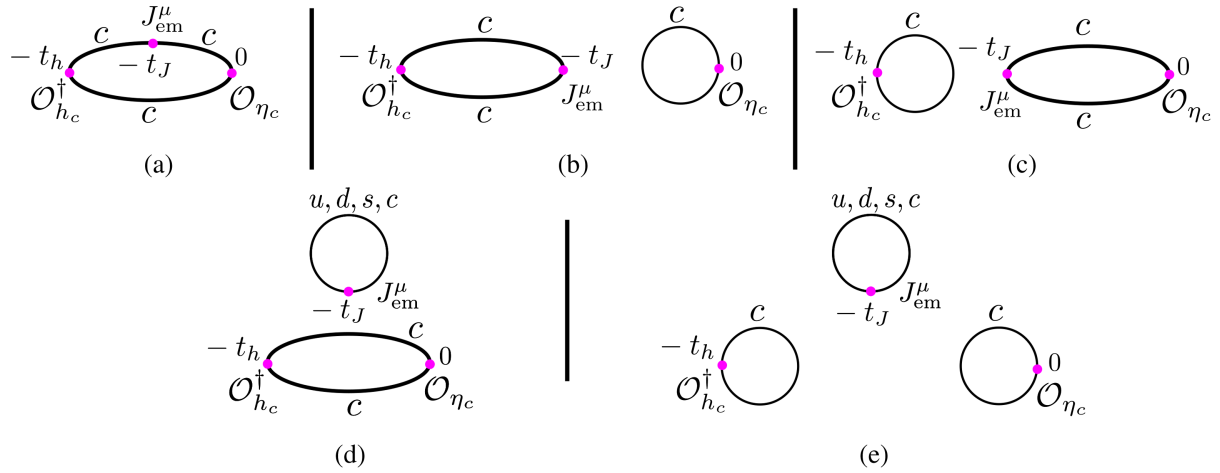

FIG. 1. Wick contractions relevant to the correlation function (6). The diagram (a) corresponds to the connected contribution, while (b), (c), (d) and (e) correspond to the disconnected ones. Diagrams (b), (c) and (e) are Zweig suppressed. For each diagram, we have indicated the flavor associated to each quark line. Light quark (u, d, s) contributions only appear in diagram (d) and diagram (e) where the photon is emitted by a sea quark. These two diagrams vanish in the SU(3)-limit $m_u = m_d = m_s$, while the effect of the c sea quark should be negligible.

$$\vec{\theta} = (0, 0, \theta_z^c), \qquad \theta_z^c = \frac{L}{\pi} \frac{m_{h_c}^2 - m_{\eta_c}^2}{2m_{h_c}}. \tag{11}$$

The connected part of $C_{3\mathrm{pt}}^{\mu}(t_h; t_J)$ is evaluated as follows.[4] By $S_c(x, y)$ and $S_c^{\theta}(x, y)$ we denote the charm quark propagators evaluated on the background field configurations corresponding to $U_\mu(x)$ and $U_\mu^{\theta}(x)$, respectively, so that $C_{3\mathrm{pt}}^{\mu}(t_h; t_J)$ can be written as,

$$C_{3\mathrm{pt}}^{\mu}(t_h, t_J) = 2 \sum_{\mathbf{x},\mathbf{y},\mathbf{z}} \langle \mathrm{Tr}[S_c(x, z) \sigma^{23} S_c(z, y) \gamma^{\mu} S_c^{\theta}(y, x) \gamma^5] \rangle, \tag{12}$$

where $x = (\mathbf{x}, 0)$, $y = (\mathbf{y}, -t_J)$, $z = (\mathbf{z}, -t_h)$. The trace $\mathrm{Tr}[\ldots]$ is taken over the color and Dirac indices, and $\langle \ldots \rangle$ indicates the average over the SU(3) gauge field configurations $U_\mu(x)$. The factor of two in Eq. (12) accounts for the contribution of the charge conjugated diagram in which the photon is emitted by the charm antiquark. The sum over $\mathbf{x}$ is evaluated stochastically by performing the inversion of the charm quark Dirac operator on a number N_{stoch} of spatial stochastic sources $\eta(w)$, placed at time $t = 0$ (stochastic time wall sources), namely

$$\begin{aligned} S_c^{\theta}(y, x) &\mapsto S_c^{\theta}(y, w) \eta(w), \\ S_c(z, x) &\mapsto S_c(z, w') \eta(w'), \end{aligned} \tag{13}$$

with $\eta(\mathbf{w}, w_0) = \delta_{w_0,0} \bar{\eta}(\mathbf{w})$, and $\langle \bar{\eta}^{\dagger}(\mathbf{w}') \bar{\eta}(\mathbf{w}) \rangle_{\eta} = \delta_{\mathbf{w}',\mathbf{w}}$. The backward propagator $S_c(x, z)$ is then obtained from $S_c(z, x)$ by using γ^5 Hermiticity. Depending on the ensemble considered, we use up to $N_{\mathrm{stoch}} = 32$ spin-diluted stochastic sources per gauge configuration. A diagrammatic representation of the strategy adopted to evaluate the connected contribution to $C_{3\mathrm{pt}}^{\mu}(t_h; t_J)$ is shown in Fig. (2).

We now discuss how the charm quark bilinears $\mathcal{O}_{\eta_c}$, $\mathcal{O}_{h_c}$, and the current J_c^{μ}, are discretized on the lattice. When evaluating the connected diagrams using the twisted mass action, there are different options when it comes to discretizing the quark bilinears and they differ in the choice of the Wilson parameter of the quark field, $r_+ = \pm 1$, and of the antiquark field, $r_- = \pm 1$. They can be chosen to be opposite ($r_+ = -r_-$) or equal ($r_+ = r_-$). The two regularizations are known as the twisted mass (TM) and Osterwalder-Seiler regularizations, respectively. The results obtained using different combinations of TM and OS bilinears differ only by $O(a^2)$ UV cutoff effects. A complete description of the two regularizations is given in Appendix B of Ref. [36] to which we refer for further details. In this calculation we opt to use the OS regularization for the electromagnetic current, while $\mathcal{O}_{\eta_c}$ and $\mathcal{O}_{h_c}$ are regularized as TM bilinears.[5] With this choice, the interpolating operators are given by

[4]To simplify the expressions we consider the case of local interpolating operators, i.e. $\kappa = 0$.

[5]This choice for the interpolating operator of the h_c meson, avoids the mixing with 1^{--} (J/Ψ) and 1^{++} (χ_{c1}) states. This is a consequence of the exact $P \times G$ symmetry, where P is parity and G is G parity, enjoyed by the TM regularization (see also Ref. [40]).

$$\mathcal{O}_{\eta_c}(\mathbf{x},t) = \sum_{\mathbf{y}} \bar{q}_c(\mathbf{x},t) G_t^{\eta}(\mathbf{x},\mathbf{y}) \gamma^5 q'_c(\mathbf{y},t),$$
$$\mathcal{O}_{h_c}(\mathbf{x},t) = \sum_{\mathbf{y}} \bar{q}_c(\mathbf{x},t) G_t^{\eta}(\mathbf{x},\mathbf{y}) \sigma^{23} q'_c(\mathbf{y},t), \quad (14)$$

and the quark action of the field $q'_c(x)$ is equal to that of the $q_c(x)$ field in Eq. (4) after replacing $r'_c = -r_c$. The charm quark component of the electromagnetic current, instead, is regularized as $J_c^{\mu}(x) = \bar{q}_c(x)\gamma^{\mu} q_c(x)$ with $r_c = 1$. With this choice, the renormalization constant of the local electromagnetic current is given by $Z_V(g_0^2)$, the value of which is given in Table I for each lattice ensemble used in this work. If we use S_c^r and $S_c^{\theta,r}$ to denote the charm quark propagators corresponding to a given value of $r = \pm 1$, then Eq. (12) gets modified by the replacements, $S_c^{\theta}(y,x) \to S_c^{\theta,+}(y,x)$, and $S_c(z,y) \to S_c^{+}(z,y)$ and $S_c(x,z) \to S_c^{-}(x,z)$. Note that the γ^5 Hermiticity of the twisted Wilson quark propagator reads,

$$S_c^{\pm\dagger}(x,y) = \gamma^5 S^{\mp}(y,x)\gamma^5. \quad (15)$$

A. Extraction of the form factor F_1^c

We first need to consider the two point functions of interpolating fields $\mathcal{O}_{\eta_c}$ and $\mathcal{O}_{h_c}$, respectively, in order to extract their mass/energy and their couplings. We define,

$$C_{2\mathrm{pt}}^{\eta_c}(t) = \sum_{\mathbf{x}} e^{i\mathbf{k}\mathbf{x}} \langle 0|\mathcal{O}_{\eta_c}(\mathbf{x},t)\mathcal{O}_{\eta_c}^{\dagger}(\mathbf{0},0)|0\rangle,$$
$$C_{2\mathrm{pt}}^{h_c}(t) = \sum_{\mathbf{x}} \langle 0|\mathcal{O}_{h_c}(\mathbf{x},t)\mathcal{O}_{h_c}^{\dagger}(\mathbf{0},0)|0\rangle, \quad (16)$$

and again neglect the Zweig suppressed disconnected contributions to $C_{2\mathrm{pt}}^{\eta_c}(t)$ and $C_{2\mathrm{pt}}^{h_c}(t)$. In the limit of large Euclidean time t, the two point correlation functions behave as,

$$C_{2\mathrm{pt}}^{\eta_c}(t) = \frac{|Z_{\eta_c}|^2}{2E_{\eta_c}} \left(e^{-E_{\eta_c} t} + e^{-E_{\eta_c}(T-t)}\right) + \ldots,$$
$$C_{2\mathrm{pt}}^{h_c}(t) = \frac{|Z_{h_c}|^2}{2m_{h_c}} \left(e^{-m_{h_c} t} + e^{-m_{h_c}(T-t)}\right) + \ldots, \quad (17)$$

where m_{h_c} and E_{η_c} are the mass and energy (due to the nonzero momentum $\mathbf{k}$) of the corresponding meson, and

$$Z_{\eta_c} = \langle 0|\mathcal{O}_{\eta_c}|\eta_c(k)\rangle, \quad Z_{h_c} = \langle h_c(p,\epsilon_\lambda)|\mathcal{O}_{h_c}^{\dagger}|0\rangle. \quad (18)$$

The ellipses in Eq. (17) denote contributions that vanish in the large time limit, $0 \ll t \ll T$. We also computed $C_{2\mathrm{pt}}^{\eta_c}(t)$ with $\mathbf{k} = \mathbf{0}$, which is needed to extract m_{η_c}.

The interpolating field $\mathcal{O}_{h_c}^{\dagger}$ in Eq. (7) creates an h_c meson with polarization $\epsilon_\lambda^{\mu} = -\delta^{\mu 1}$. Since we chose $q^1 = p^1 = 0$, it is then straightforward to use Eq. (1) and combine the above mentioned quantities into

$$\bar{F}_1^c(t_h;t_J) = \frac{iZ_V(g_0^2)}{2Q_c} \frac{4E_{\eta_c}}{Z_{\eta_c} Z_{h_c}} e^{E_{\eta_c} t_J} e^{m_{h_c}(t_h - t_J)} C_{3\mathrm{pt}}^{1}(t_h;t_J), \quad (19)$$

which, for large Euclidean time separations, gives the desired form factor $F_1^c \equiv F_1^c(0)$,

$$\bar{F}_1^c(t_h;t_J) \xrightarrow[t_h - t_J \to \infty]{t_J \to \infty} F_1^c. \quad (20)$$

Note again that we included $Z_V(g_0^2)$ in Eq. (19), the values of which are listed in Table I.

As already discussed in the previous Section, and illustrated in Fig. 2, we compute $C_{3\mathrm{pt}}^{\mu}(t_h;t_J)$ by placing the interpolating field of the η_c meson at a fixed time $t = 0$, the charm quark component of the electromagnetic current is then inserted in a charm quark line at a fixed $-t_J < 0$, while the time $-t_h \ll -t_J$, at which the h_c is created, corresponds to the *sink* of the correlation function, which is thus known for all times $-t_h$. This allows us to carefully monitor the onset of the dominance of the h_c state. Since in our computational setup the time t_J is fixed, we must ensure we choose a sufficiently large t_J to be able to isolate the η_c meson state. The advantage of placing the interpolator corresponding to η_c at the source of the correlation function is that t_J can be chosen reasonably large without a significant loss of the signal, since the signal-to-noise ratio (S/N) of $C_{3\mathrm{pt}}^{\mu}(t_h;t_J)$ practically only depends on the time distance $|t_J - t_h|$.[6] As it will be detailed in the next subsection, we have considered two different values for $t_J \simeq 1.6, 2.4$ fm, and checked that no difference in the results for $\bar{F}_1^c(t_h;t_J)$ are visible within statistical uncertainties.

B. Numerical results

On all the ETMC gauge ensembles listed in Table I we computed the correlation functions $C_{2\mathrm{pt}}^{h_c}(t)$, $C_{2\mathrm{pt}}^{\eta_c}(t)$ and $C_{3\mathrm{pt}}^{\mu}(t_h;t_J)$. In Fig. 3 we show the effective mass plots for η_c and h_c mesons, for all the lattice spacings. Note that since the charm quark mass has been fixed by $m_{D_s} = 1967$ MeV at each value of the lattice spacing, due to the finite lattice artifacts the values of m_{η_c} and m_{h_c} are not the same for all ensembles. Owing to the fact that η_c is the

[6] For a fixed $t_J - t_h$, according to the Parisi-Lepage theorem, the S/N ratio of $C_{3\mathrm{pt}}^{\mu}(t_h;t_J)$ scales as $e^{-(E_{\eta_c} - m_{\eta_c})t_J} \simeq e^{-|\mathbf{k}|^2 t_J/2m_{\eta_c}}$, with $|\mathbf{k}|^2/2m_{\eta_c} \simeq 40$ MeV. The S/N ratio thus decreases very slowly as t_J increases. In the bottomonium case, to be discussed in the next Section, the deterioration of the signal is even milder because the momentum transfer $|\mathbf{k}|$ is still of $O(500$ MeV) but $m_{\eta_b} \simeq 9.4$ GeV.

lightest charmonium state the S/N ratio of $C^{\eta_c}_{\rm 2pt}(t)$ does not decrease with t, as is clear from Fig. 3. This is in contrast to the case of $C^{h_c}_{\rm 2pt}(t)$, for which the effective mass becomes exponentially noisier as the time t increases. To estimate the systematic error on m_{h_c}, we additionally evaluated the smeared-local correlation function of the h_c meson, which is obtained by replacing one Gaussian-smeared operator $\mathcal{O}^\dagger_{h_c}$ in Eq. (7) by the local one ($\kappa = 0$). The difference between the effective mass plateaus obtained by considering the smeared-local and smeared-smeared correlation functions has been included in systematic uncertainty. The colored bands in Fig. 3 already account for that systematics. Note that the larger error for the A48 ensemble is due to uncertainty on the lattice spacing of that ensemble ($\simeq$0.6%). The extrapolation to the continuum limit of the lattice results for m_{η_c} and m_{h_c} is shown in Fig. 4. The continuum fits are performed both linearly and quadratically in a^2. These two fits are then combined via the Bayesian Akaike Information Criterion (BAIC) [41], the method which we now briefly summarize. Let $x_1, \ldots, x_N$ be the outcomes of N different fits. The final central value and the total error are given by

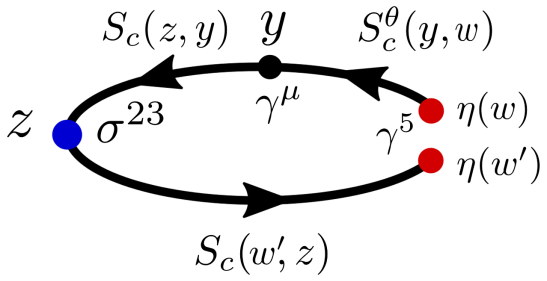

FIG. 2. Schematic representation of the strategy adopted to evaluate the connected contribution to $C^{\mu}_{\rm 3pt}(t_h; t_J)$. The sum over $\mathbf{x}$ is implemented stochastically by inverting the charm quark Dirac operator on a number $N_{\rm stoch}$ of the spatial stochastic sources η (red vertices). The electromagnetic current is inserted in the upper quark line at the fixed time $-t_J$ (black vertex) and at all spatial positions $\mathbf{y}$. The blue vertex indicates $z = (\mathbf{z}, -t_h)$, where the h_c meson is created.

$$\bar{x} = \sum_{n=1}^{N} w_n x_n, \qquad \sigma^2 = \sigma^2_{\rm stat} + \sum_{n=1}^{N} w_n (x_n - \bar{x})^2, \quad (21)$$

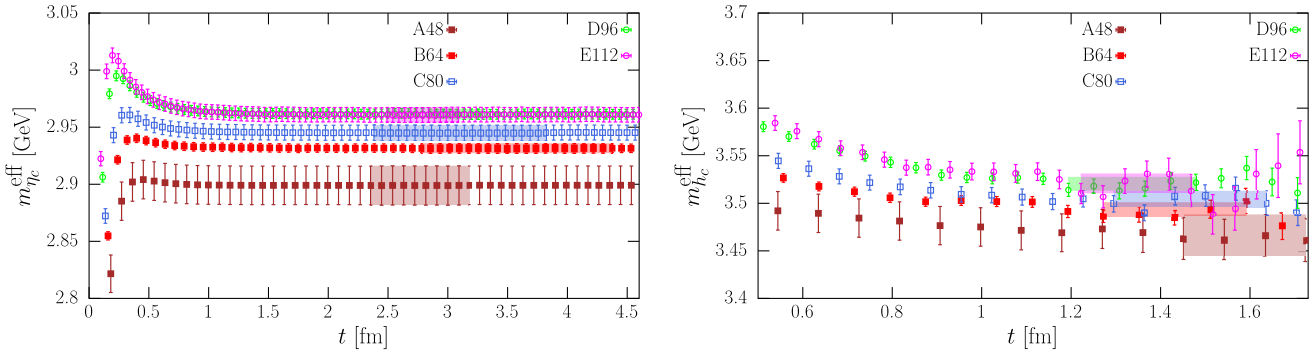

FIG. 3. Effective mass of the η_c meson (left) and of the h_c meson (right) for all five gauge ensembles used for the present calculation. The colored bands correspond to our estimate of the η_c and h_c masses on each ensemble.

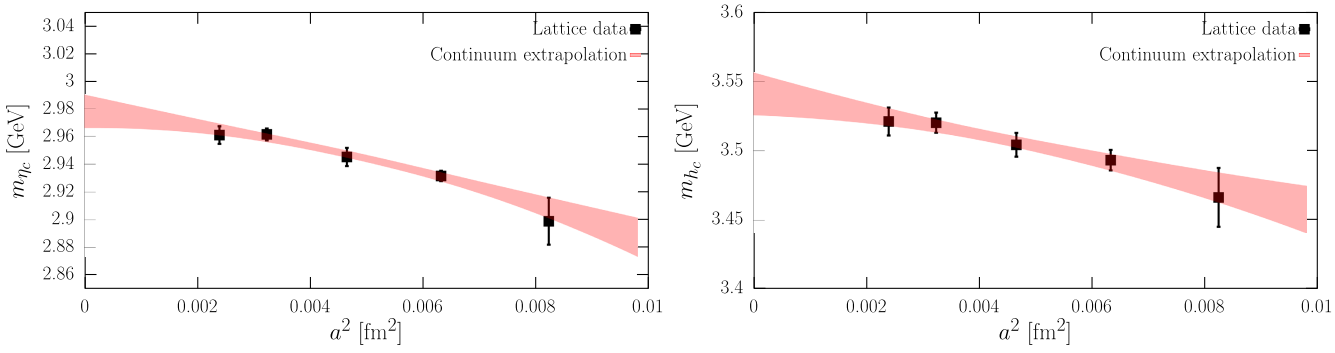

FIG. 4. Extrapolation of η_c (left) and h_c (right) masses to the continuum limit ($a \to 0$). The colored bands correspond to the best fit obtained after performing linear and quadratic fits in a^2, and then combining them using the BAIC. The reduced χ^2 of all the fits are always below one.

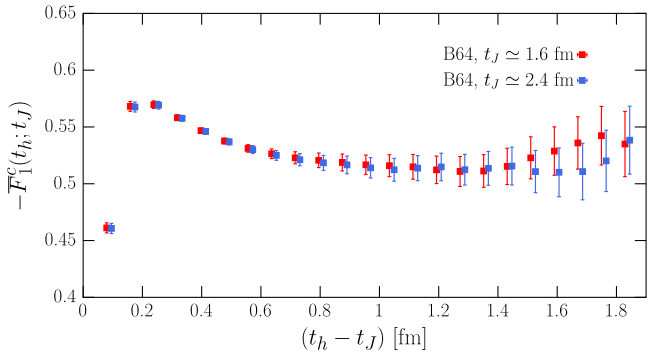

FIG. 5. Comparison between $\bar{F}_1^c(t_h, t_J)$ with $t_J \simeq 1.6$ fm (red) and with $t_J \simeq 2.4$ fm (blue) on the B64 ensemble. The data points at $t_J \simeq 2.4$ fm have been slightly shifted horizontally for easier comparison.

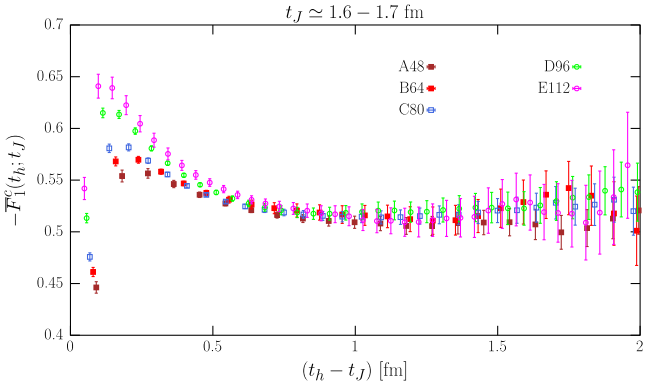

FIG. 6. Function $\bar{F}_1^c(t_h; t_J)$, defined in Eq. (19), as obtained for all lattice ensembles, cf. Table I, and for t_J fixed as discussed in the text.

where σ_{stat} is the statistical error of $\bar{x}$, and $w_1, \ldots, w_N$ are the weights normalized to one and given by

$$w_n \propto \exp[-(\chi_n^2 + 2N_n^{\text{pars}} - 2N_n^{\text{data}})], \tag{22}$$

with χ_n^2 being the chi-squared of the n-th fit, with its corresponding number of free parameters (N_n^{pars}) and of the data points (N_n^{data}).

In the continuum limit we obtain

$$m_{\eta_c} = 2.978(12)\,\text{GeV}, \quad m_{h_c} = 3.541(15)\,\text{GeV}, \tag{23}$$

which agree very well with the current experimental values, $m_{\eta_c}^{\text{exp}} = 2.9841(4)$ GeV and $m_{h_c}^{\text{exp}} = 3.52537(14)$ GeV [9]. These results also suggest that the impact of neglecting the annihilation diagrams in $C_{2\text{pt}}^{\eta_c}$ and in $C_{2\text{pt}}^{h_c}(t)$ is small, i.e. of the order of our statistical uncertainty which is about 0.4% for both m_{η_c} and m_{h_c}. This is also in line with Ref. [39] where the contribution of the disconnected diagram to m_{η_c} was found to be about $+7(1)$ MeV.

We now turn to our determination of F_1^c, starting with a discussion on the tuning of the momentum $\mathbf{k}$ of the η_c at nonzero lattice spacing. The relation in Eq. (5) can be used by either plugging in m_{η_c} and m_{h_c} obtained at each lattice spacing, or by using the experimental results, which, as we have just shown, agree well with our continuum extrapolated results in Eq. (23). These two choices lead to determinations of F_1^c that differ only by $O(a^2)$ UV cutoff effects. We opt for $m_{\eta_c}^{\text{exp}}$ and $m_{h_c}^{\text{exp}}$ and tune the momentum $\mathbf{k}$ for each lattice spacing.

As already anticipated, in our calculation of the correlation function $C_{3\text{pt}}^{\mu}(t_h; t_J)$, the time $-t_J$ of the transition operator is always fixed, while t_h runs over the lattice. It is thus important to choose sufficiently large t_J in order to ensure the dominance of η_c. We carried out a test on the B64 ensemble, and computed $C_{3\text{pt}}^{\mu}(t_h; t_J)$ for two different values of $t_J \sim 1.6, 2.4$ fm. In Fig. 5 we compare the corresponding $\bar{F}_1^c(t_h; t_J)$, cf. Eq. (19). Clearly, the two results are in excellent agreement. The difference in statistical uncertainties between the two cases is consistent with expectations of S/N of $C_{3\text{pt}}^{\mu}(t_h, t_J)$ as a function of t_J (with $t_J - t_h$ fixed), as discussed at the end of the previous subsection. On the basis of these observations we decided to fix $t_J \simeq 1.7$ fm for all other ensembles.

In Fig. 6 we show $\bar{F}_1^c(t_h; t_J)$ for all our lattices. Quite remarkably, the UV cutoff effects are very small, and the results at all lattice spacings are in agreement within statistical errors. That feature has already been observed in Ref. [30] in which the twisted mass Wilson quarks were used but without the Clover term. We then extract the form factor F_1^c by fitting $\bar{F}_1^c(t_h; t_J)$ to a constant in the time interval $t_J - t_h \in (0.9, 1.3)$ fm.

The results of F_1^c are presented in Table II. We then extrapolate these results to the continuum limit by a simple linear a^2 fit, cf. Fig. 7. The corresponding $\chi^2/\text{dof} \simeq 0.2$ is very good and our final result for the form factor describing $h_c \to \eta_c \gamma$ is

$$\boxed{F_1^c = -0.522(10).} \tag{24}$$

TABLE II. Values of the form factor F_1^c for each gauge ensemble employed for the present calculation.

a (fm)	0.0907(5)	0.07948(11)	0.06819(14)	0.056850(90)	0.04892(11)
$-F_1^c$	0.5077(74)	0.514(12)	0.5148(64)	0.5197(88)	0.512(12)

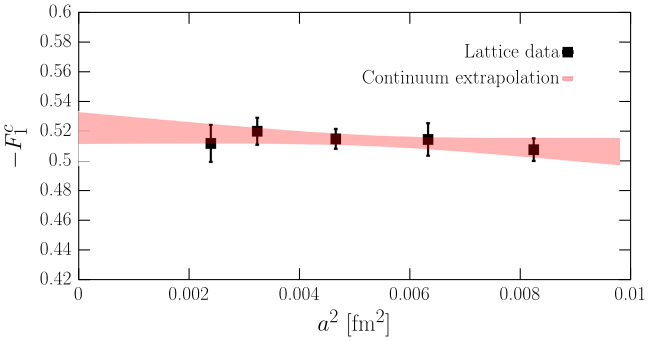

FIG. 7. Continuum-limit extrapolation of the form factor F_1^c. The colored band corresponds to the best-fit function obtained after performing a linear fit in a^2 to our lattice data. The reduced χ^2 of the fit is around 0.2.

The uncertainty is more than twice smaller than the one reported in Ref. [30]. In Sec. IV, we will compare our result for F_1^c with existing theoretical determinations and with the available experimental results. We now turn to the analysis of the $h_b \to \eta_b\gamma$ decay.

III. CALCULATION OF THE $h_b \to \eta_b\gamma$ TRANSITION FORM FACTOR

Analogously to Eq. (1) the transition matrix element describing $h_b \to \eta_b\gamma^*$ is decomposed as

$$\begin{aligned}&\langle\eta_b(k)|J^\mu_{\rm em}|h_b(p,\varepsilon_\lambda)\rangle\\&= 2iQ_b\left\{m_{h_b}F_1^b(q^2)\left(\epsilon^{*\mu}_\lambda - \frac{\epsilon^*_\lambda\cdot q}{q^2}q^\mu\right)\right.\\&\left.+ F_2^b(q^2)(\epsilon^*_\lambda\cdot q)\left[\frac{m^2_{h_b}-m^2_{\eta_b}}{q^2}q^\mu - (p+k)^\mu\right]\right\},\end{aligned} \tag{25}$$

and the decay rate for the on-shell photon corresponding to $q^2 = 0$ is given by ($F_1^b \equiv F_1^b(0)$)

$$\Gamma(h_b\to\eta_b\gamma) = \frac{2Q_b^2}{3}\alpha_{\rm em}\frac{m^2_{h_b}-m^2_{\eta_b}}{m_{h_b}}|F_1^b|^2, \tag{26}$$

where, as before, we use $F_1^b \equiv F_1^b(0)$, for shortness. We again neglect the disconnected contributions so that only the b-quark component of the electromagnetic current contributes to the matrix element and in Eq. (25) one can replace

$$J^\mu_{\rm em}(x) \mapsto J^\mu_b(x) = Q_b\bar{q}_b(x)\gamma^\mu q_b(x). \tag{27}$$

In the rest frame of h_b ($\mathbf{p} = 0$) the three momentum $\mathbf{k}$ of the η_b that corresponds to $q^2 = 0$ is

$$|\mathbf{k}| = \frac{m^2_{h_b}-m^2_{\eta_b}}{2m_{h_b}} \simeq 488\ \text{MeV}, \tag{28}$$

which differs from the momentum $\mathbf{k}$ of the η_c meson in Eq. (5) by only 12 MeV.

Like we already mentioned in the Introduction, the $h_b \to \eta_b\gamma$ decay cannot be directly accessed from our lattices because the physical b-quark mass is too heavy and we therefore evaluate the $h_b \to \eta_b\gamma$ transition form factor F_1^b by working with a series of heavy quark masses $m_H^{(n)}$ (with $am_H^{(n)} \lesssim 0.5$) and then extrapolate the results to the physical point corresponding to $m_H \to m_b$. In Table III we give the masses of simulated heavy quarks for each of the lattice ensembles used in this work. Note that the heavy quark masses $m_H^{(n)}$ satisfy

$$am_H^{(n+1)} = \lambda am_H^{(n)} \tag{29}$$

with $\lambda = 1.24283$, $n = 1,\ldots,6$, and $am_H^{(1)} = am_c$.[7] The parameter λ is chosen in such a way that $m_b/m_c \simeq \lambda^7 = 4.58$ [42]. The lattice setup used to extract the transition form factor for each heavy quark mass $m_H^{(n)}$ is essentially identical to that employed for $h_c \to \eta_c\gamma$ and described in the previous Section.

In the following we denote by η_H and h_H the fictitious states similar to η_c and h_c but with the heavy quark m_H instead of m_c. As before, for each heavy quark mass, the three-momentum $\mathbf{k}$ given to η_H is set to the value of Eq. (28) for each of the gauge ensembles, and not to that corresponding to the $h_H \to \eta_H\gamma$ decay. The difference between the transition form factors obtained by rescaling or not rescaling the momentum $\mathbf{k}$ is entirely negligible, as we verified explicitly for $m_H = m_c$ where the deviation would be more pronounced (see Sec. III B).

The interpolating operators of the η_H ($\mathcal{O}_{\eta_H}$) and of the h_H ($\mathcal{O}_{h_H}$) meson are defined as in Eqs. (7), (14) with $q_c(x) \mapsto q_H(x)$. In order to improve the overlap with the ground state we tuned the number of smearing steps $n(m_H)$ for each mass m_H so as to ensure a smearing radius

$$r_0(m_H) = \frac{an(m_H)}{\sqrt{\kappa^{-1}+6}} \simeq \left(\frac{m_c}{m_H}\right)\times 0.15\ \text{fm}. \tag{30}$$

Like in the previous Section we compute the two point functions

$$\begin{aligned}C^{\eta_H}_{\rm 2pt}(t) &= \sum_{\mathbf{x}} e^{i\mathbf{kx}}\langle 0|\mathcal{O}_{\eta_H}(\mathbf{x},t)\mathcal{O}^\dagger_{\eta_H}(\mathbf{0},0)|0\rangle,\\ C^{h_H}_{\rm 2pt}(t) &= \sum_{\mathbf{x}}\langle 0|\mathcal{O}_{h_H}(\mathbf{x},t)\mathcal{O}^\dagger_{h_H}(\mathbf{0},0)|0\rangle,\end{aligned} \tag{31}$$

[7]At the heaviest simulated quark mass $m_h/m_c \simeq 3$ we decided to include the results on the C80 ensemble where $am_H^{(6)} \simeq 0.588$ is slightly larger than 0.5.

TABLE III. Bare heavy quark masses $am_H^{(n)}$ used for the calculation of the $h_b \to \eta_b\gamma$ transition form factor, for all of the gauge ensembles used in this calculation, specified in Table I.

ID	$am_H^{(1)}$	$am_H^{(2)}$	$am_H^{(3)}$	$am_H^{(4)}$	$am_H^{(5)}$	$am_H^{(6)}$
A48	0.26200	0.32562	0.40469	0.50296	//	//
B64	0.23157	0.28780	0.35769	0.44455	//	//
C80	0.19840	0.24658	0.30645	0.38087	0.47336	0.58830
D96	0.16490	0.20494	0.25471	0.31656	0.39343	0.48897
E112	0.14125	0.17555	0.21818	0.27116	0.33700	0.41884

in which the annihilation contributions have been neglected and extract m_{h_H} and E_{η_H}, and the quantities

$$Z_{\eta_H} = \langle 0|\mathcal{O}_{\eta_H}|\eta_H(k)\rangle, \quad Z_{h_H} = \langle h_H(p,\epsilon_\lambda)|\mathcal{O}^\dagger_{h_H}|0\rangle. \tag{32}$$

We also computed $C^{\eta_H}_{2\mathrm{pt}}(t)$ with $\mathbf{k} = 0$, which is needed to get m_{η_H}. Finally, the three point function corresponding to the connected diagram, needed for the determination of the transition form factor, is given by

$$\begin{aligned} C^\mu_{3\mathrm{pt}}(t_h; t_J, m_H) &= \sum_{\mathbf{x},\mathbf{y},\mathbf{z}} e^{i\mathbf{k}(\mathbf{x}-\mathbf{y})}\langle 0|\mathcal{O}_{\eta_H}(\mathbf{x},0)J^\mu_H(\mathbf{y},-t_J) \\ &\quad \times \mathcal{O}^\dagger_{h_H}(\mathbf{z},-t_h)|0\rangle_{\mathrm{conn}}, \\ &= 2\sum_{\mathbf{x},\mathbf{y},\mathbf{z}} \langle \mathrm{Tr}[S_H(x,z)\sigma^{12}S_H(z,y) \\ &\quad \times \gamma^\mu S^\theta_H(y,x)\gamma^5]\rangle, \end{aligned} \tag{33}$$

where $J^\mu_H(x) = Q_b\bar{q}_H(x)\gamma^\mu q_H(x)$, and $S^\theta_H(x,y)$ is the heavy quark propagator computed on the gauge background $U^\theta_\mu(x)$ as discussed in Eq. (10). Note that $S_H(x,y)$ corresponds to $|\vec{\theta}| = 0$. The twisting angle $\vec{\theta}$ is again chosen to produce the momentum specified in Eq. (28).

A. Numerical results for m_{η_H} and m_{h_H}

For each of the heavy quark masses, listed in Table III, we compute the corresponding m_{η_H} and m_{h_H}. The quality of the effective mass plateaus is illustrated in Fig. 8 where we plot the difference between effective masses of the η_H (h_H) at two consecutive heavy quark masses, $m_H^{(n)}$ and $m_H^{(n-1)}$. The results shown correspond to our determination on the finest lattice spacing ensemble employed in this calculation. From a fit to a constant for large time separations we extract the mass differences,

$$\begin{aligned} \Delta m^{(n)}_{\eta_H} &= m_{\eta_H}\left(m_H^{(n)}\right) - m_{\eta_H}\left(m_H^{(n-1)}\right), \\ \Delta m^{(n)}_{h_H} &= m_{h_H}\left(m_H^{(n)}\right) - m_{h_H}\left(m_H^{(n-1)}\right), \end{aligned} \tag{34}$$

where we indicated with $m_{\eta_H}(m_H)$ and $m_{h_H}(m_H)$ the masses of the η_H and h_H meson evaluated at a given heavy-quark mass m_H. As in the case of the h_c mass, the difference between the effective mass plateaus obtained using smeared-smeared and smeared-local correlation functions is included in systematic uncertainty of our estimate of $\Delta m^{(n)}_{h_H}$. The colored bands in the left plot of Fig. 8 are already include this systematic error. As it can be appreciated in Fig. 8, the values of $\Delta m^{(n)}_{\eta_H}$ and $\Delta m^{(n)}_{h_H}$ are

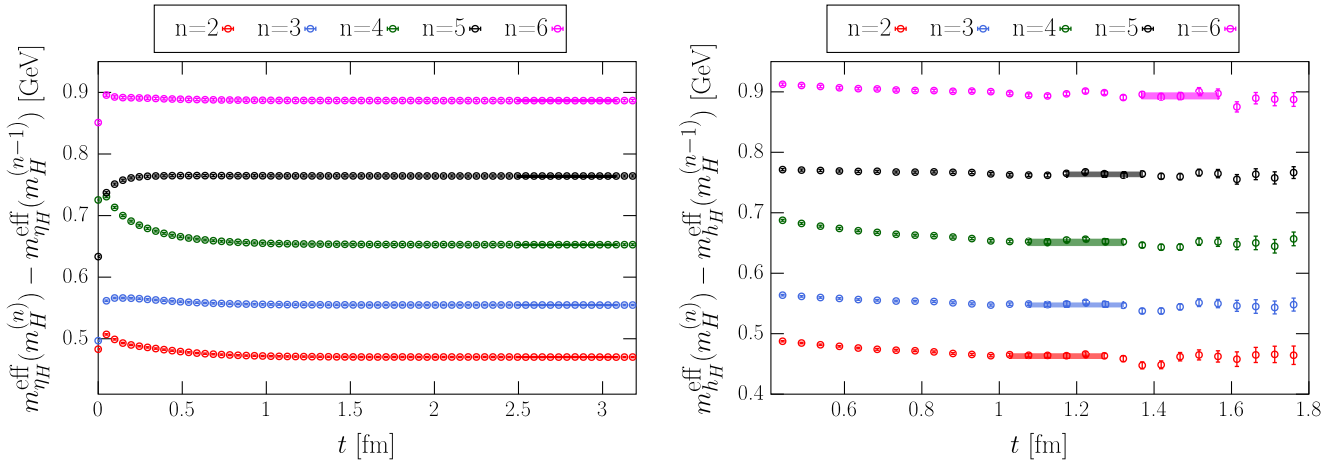

FIG. 8. Difference between the effective mass of the η_H (left) and h_H meson (right), evaluated for two successive values of the heavy quark masses $m_H^{(n)}$ and $m_H^{(n-1)}$ for $n = 2, 3, 4, 5, 6$. The illustrated results correspond to our finest lattice ensemble (E112 in Table I).

quite similar, consistent with what is known from the experiment where $m_{h_b}^{\rm exp} - m_{h_c}^{\rm exp} \simeq 6.37$ GeV is very close to $m_{\eta_b}^{\rm exp} - m_{\eta_c}^{\rm exp} \simeq 6.41$ GeV, thus differing by only 40 MeV.

While the quality of the plateaus is always excellent for η_H, in the case of h_H the S/N of $C_{\rm 2pt}^{h_H}(t)$ is expected to decrease over time as $e^{-(m_{h_H}-m_{\eta_H})t} \simeq e^{-(500\ {\rm MeV})t}$, independently on the heavy quark mass m_H. However, when considering the correlated difference between the effective mass of h_H computed with two consecutive heavy quark masses, the statistical errors partially cancel (because the S/N is largely independent on the heavy quark mass m_H in the simulated region) and the quality of the plateaus substantially improves, allowing us to better identify the time interval where to perform a constant fit to our data. This is highlighted by the colored bands in the right panel of Fig. 8. The masses of the h_H mesons are determined this way: we first evaluate on each ensemble the mass differences $\Delta m_{h_H}^{(n)}$ and then reconstruct $m_{h_H}(m_H^{(n)})$ as

$$m_{h_H}(m_H^{(n)}) = m_{h_c} + \begin{cases} \sum_{i=2}^{n} \Delta m_{h_H}^{(i)}, & \text{if} \quad n \geq 2 \\ 0, & \text{otherwise} \end{cases}. \tag{35}$$

To extrapolate m_{η_H} and m_{h_H} to the continuum limit for each simulated heavy quark mass m_H, we follow two different strategies. In the first, we take the continuum limit of both m_{η_H} and m_{h_H}, for each value of the heavy-quark mass m_H, by using the *Ansatz*

$$\begin{aligned} m_{\eta_H}(m_H, a) &= A_0(m_H) + A_1(m_H)a^2 + A_2(m_H)a^4, \\ m_{h_H}(m_H, a) &= B_0(m_H) + B_1(m_H)a^2 + B_2(m_H)a^4, \end{aligned} \tag{36}$$

where distinct fit parameters, $A_0(m_H)$, $A_1(m_H)$, $A_2(m_H)$, $B_0(m_H)$, $B_1(m_H)$, $B_2(m_H)$ are used for each m_H value. We perform both linear and quadratic fits in a^2, which are then combined using the BAIC. For the two heaviest heavy quark mass $m_H = \lambda^4 m_c$ and $m_H = \lambda^5 m_c$, where the results only at three lattice spacings are available (C80, D96 and E112) we perform a simple linear a^2 fit [$A_2(m_H) = B_2(m_H) = 0$]. We never impose a prior on any of the fit parameters.

Our second strategy is to perform a global fit that simultaneously describes the dependence on lattice artifacts according to,

$$\begin{aligned} m_{\eta_H}(m_H, a) &= A'_0(m_H) \times (1 + A'_1 a^2 + A'_{1,m} a^2 m_H^2 + A'_2 a^4 \\ &\quad + A'_{2,m} a^4 m_H^2 + A'_{2,m_2} a^4 m_H^4), \\ m_{h_H}(m_H, a) &= B'_0(m_H) \times (1 + B'_1 a^2 + B'_{1,m} a^2 m_H^2 + B'_2 a^4 \\ &\quad + B'_{2,m} a^4 m_H^2 + B'_{2,m_2} a^4 m_H^4), \end{aligned} \tag{37}$$

where $A'_0(m_H)$ and $B'_0(m_H)$ are fit parameters specific for each heavy quark mass, while the remaining parameters $A'_{1,2}$ and $B'_{1,2}$ describe the cutoff effects and are common to all the simulated heavy quark masses. This form already provides a good description of the data with $A'_{2,m_2} = B'_{2,m_2} = 0$.

Illustration of how these two strategies compare is provided in Fig. 9. In each plot, red and blue data points represent the lattice values of m_{η_H} and m_{h_H}, respectively. The darker bands show the separate continuum extrapolations. The quality of the fit is excellent, with at least one of the linear or quadratic fits in a^2 giving a reduced χ^2 close to unity. The lighter bands represent the corresponding results of the global fits (with $A'_{2,m_2} = B'_{2,m_2} = 0$). When five lattice spacings are available for a given m_H, the two strategies agree very well. However, when only three lattice spacings are available (for the two heaviest quark masses), the results for m_{η_H}, obtained using the two strategies, differ by a few percent (we also note that the χ^2/dof of the linear fit, for the heaviest simulated heavy quark mass, is not very good, about 2.5).

For the first four simulated heavy quark masses we take as our final results for m_{η_H} and m_{h_H} the determinations obtained performing separate fits for each heavy-quark mass. For the two heaviest masses, $m_H = \lambda^4 m_c$ and $m_H = \lambda^5 m_c$, while we consider more solid the results of the global fit, we decided to stay on the more conservative side and combine the results of both strategies using Eq. (21), assigning equal weights to the two results in the continuum limit. In Table IV, we give m_{η_H} and m_{h_H} in the continuum limit for each simulated heavy quark mass m_H.[8]

B. Numerical results for $h_H \to \eta_H \gamma$

We now discuss the determination of the amplitude for the process $h_H \to \eta_H \gamma$. Like in the previous Section we compute the three point correlation function $C_{\rm 3pt}^{\mu}(t_h; t_J, m_H)$ for every heavy quark mass $m_H^{(n)}$ given in Table III and on all of the ETMC ensembles of gauge field configurations, cf. Table I. For each $m_H^{(n)}$ we fix the three-momentum $\mathbf{k}$ of the η_H to the value indicated in Eq. (28), corresponding to the physical momentum of the η_b in the $h_b \to \eta_b \gamma$ decay. This choice does not precisely match that of the $h_H \to \eta_H \gamma$ decay, so it corresponds to a nonzero photon off shellness q^2 for $m_H < m_b$. This, however, is not a source of problems because at the physical point $m_H = m_b$, the off shellness q^2 extrapolates to its correct, vanishing, value. Furthermore, by comparing the results for $m_H = m_c$ obtained using the three-momentum $\mathbf{k}$ corresponding to $h_c \to \eta_c \gamma$ with that corresponding to $h_b \to \eta_b \gamma$, the difference between rescaling or not k is far below our uncertainties and therefore completely negligible. In what follows, we denote by $F_1(m_H)$ the form factor extracted from the three-point function $C_{\rm 3pt}^{\mu}(t_H; t_J, m_H)$ with $\mathbf{k}$ set as in Eq. (28).

[8] An alternative approach, which we did not pursue in this work, would be to compute the heavy quarkonium masses at all lattice spacings and then attempt isolating the $O(a^4)$ effects.

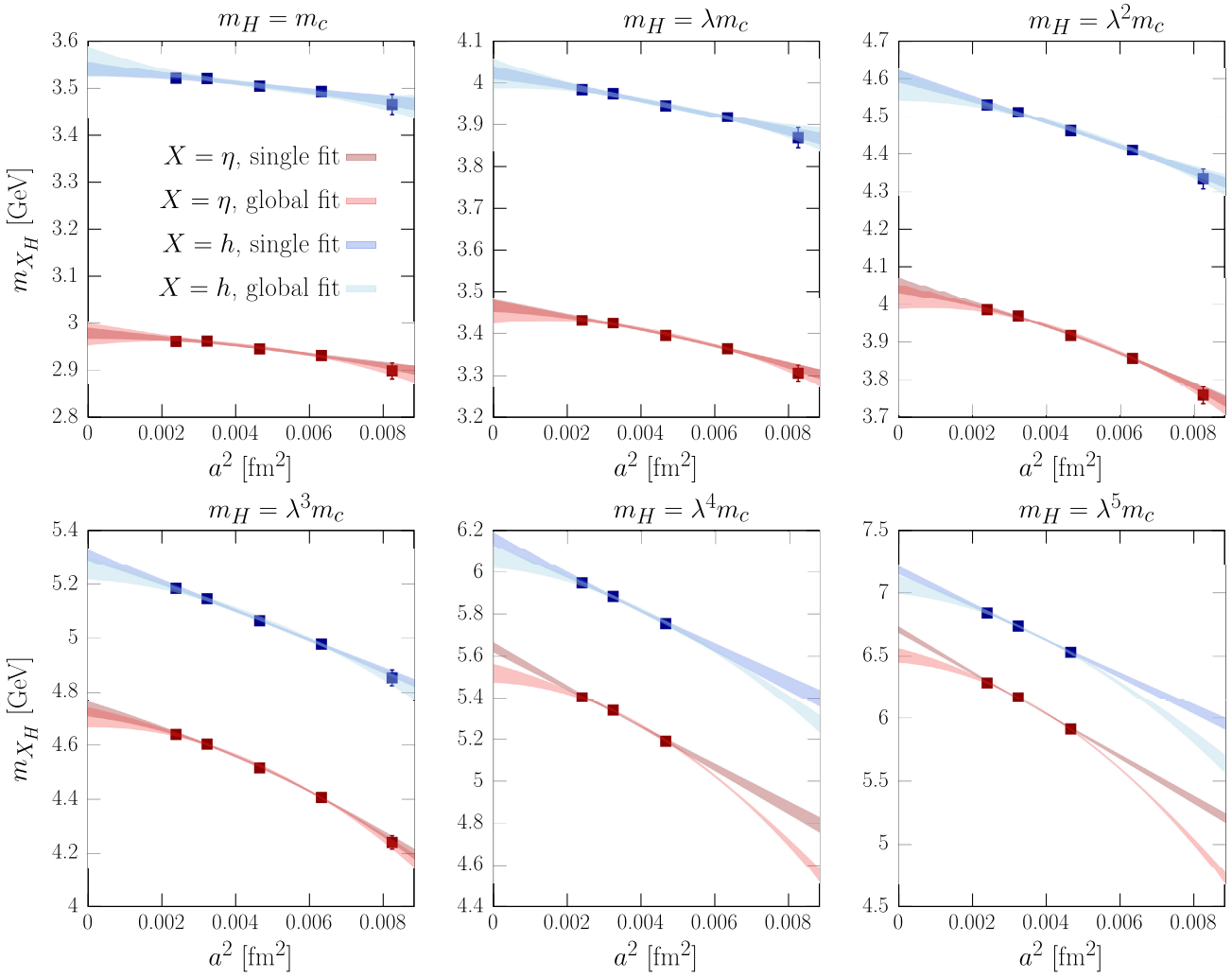

FIG. 9. Continuum extrapolation of the η_H and h_H masses, for all six simulated heavy quark masses m_H. In each plot, red and blue data points represent the lattice values of m_{η_H} and m_{h_H}. The darker bands show the results of the separate a^2 and $a^2 + a^4$ fits combined using the BAIC as described in the text. Note that for the two heaviest quark masses, where only results at three lattice spacings are available, we perform only the linear a^2 fit. The lighter bands correspond to the results of the global fit performed using Eq. (37).

On each gauge ensemble, instead of directly determining the form factor $F_1(m_H)$ for each simulated value of m_H, we find it useful to consider the ratios of form factors evaluated at two successive values, $m_H^{(n)}$ and $m_H^{(n-1)}$, of the heavy-quark mass, namely

$$r_\lambda(m_H^{(n)}) \equiv F_1\left(m_H^{(n)}\right)/F_1\left(\lambda^{-1} m_H^{(n)}\right). \tag{38}$$

The ratios $r_\lambda(m_H)$ can be extracted from the following estimator built in term of the ratio of three-point functions

$$\bar{r}_\lambda^{(n)}(t_h; t_J) = R_{h\eta}^{(n)} \exp\left\{\Delta E_{\eta_H}^{(n)} t_J\right\} \exp\left\{\Delta m_{h_H}^{(n)}(t_h - t_J)\right\} \times \frac{C_{3\mathrm{pt}}^1\left(t_h; t_J, m_H^{(n)}\right)}{C_{3\mathrm{pt}}^1\left(t_h; t_J, m_H^{(n-1)}\right)}, \tag{39}$$

$$r_\lambda(m_H^{(n)}) = \lim_{t_J \to \infty} \lim_{t_h - t_J \to \infty} \bar{r}_\lambda^{(n)}(t_h; t_J), \tag{40}$$

where

$$\Delta E_{\eta_H}^{(n)} = E_{\eta_H}(m_H^{(n)}) - E_{\eta_H}(m_H^{(n-1)}),$$
$$R_{h\eta}^{(n)} = \frac{E_{\eta_H}(m_H^{(n)})}{E_{\eta_H}(m_H^{(n-1)})} \times \frac{Z_{\eta_H}(m_H^{(n-1)})}{Z_{\eta_H}(m_H^{(n)})} \times \frac{Z_{h_H}(m_H^{(n-1)})}{Z_{h_H}(m_H^{(n)})}, \tag{41}$$

already defined in Eq. (32) at a given m_H.

Considering ratios of form factors at nearby masses provides several advantages. First, in the ratios statistical errors are reduced and only the mass difference $\Delta m_{h_H}^{(n)}$ enters the exponential terms in Eq. (39). As discussed above, the uncertainties of the differences of effective h_H

TABLE IV. Masses of η_H and h_H after extrapolation to the continuum limit. Note that the heavy quark mass $m_H^{(n)} = \lambda^n m_c$, with $\lambda = 1.24283$.

	$m_H^{(1)}$	$m_H^{(2)}$	$m_H^{(3)}$	$m_H^{(4)}$	$m_H^{(5)}$	$m_H^{(6)}$
m_{η_H} (GeV)	2.978(12)	3.467(15)	4.049(20)	4.735(29)	5.581(70)	6.61(11)
m_{h_H} (GeV)	3.541(15)	4.025(16)	4.607(17)	5.309(20)	6.116(58)	7.123(77)

masses are reduced and the plateaus are more stable compared to that of the h_H mass itself. Furthermore, the mass independent cutoff effects cancel in the ratio, thereby reducing the lattice artifacts. We therefore compute the ratios $r_\lambda(m_H^{(n)})$ on each gauge ensemble, and extrapolate them to the continuum limit. Then, having extracted $F_1(m_c)$ by the same procedure described in Sec. II [but fixing the η_c three-momentum to Eq. (28) rather than Eq. (5)], we reconstruct $F_1(m_H^{(n)})$ as

$$F_1(m_H^{(n)}) = F_1(m_c) \times \prod_{i=2}^{n} r_\lambda(m_H^{(i)}), \qquad n > 1. \tag{42}$$

The idea of considering ratios of form factors at consecutive heavy quark masses is not new. It was introduced in Ref. [33] in the context of heavy-light systems, and it is nowadays known as the *ratio method*. It has been successfully applied to the calculation of a variety of B-physics observables, including the b-quark mass m_b [43,44], the $B^{(*)}$- and $B_s^{(*)}$-meson decay constant [43–46], $B_s \to D_s$ semileptonic form factors [47,48], and the bag parameter describing $B^0 - \bar{B}^0$ mixing [45]. For the heavy-light systems the ratio method allows one to turn the extrapolation $m_H \to m_b$ to an interpolation. Indeed, owing to the fact that heavy quark effective theory predicts asymptotic power law scaling for the observables related to heavy-light hadrons O_{lh}, namely $O_{lh} \propto m_H^\alpha$ up to corrections proportional to powers of Λ/m_H, by constructing the following ratio:

$$r_\lambda^{O_{hl}}(m_H) = \lambda^{-\alpha} \frac{O_{hl}(m_H)}{O_{hl}(m_H/\lambda)}, \tag{43}$$

one has that $\lim_{m_H \to \infty} r_\lambda^{\mathcal{O}_{hl}}(m_H) = 1$, thereby turning the extrapolation to the physical point $m_H \to m_b$ into an interpolation ($r_\lambda^{O_{hl}}(\infty) = 1$). Having parametrized the mass dependence of $r_\lambda^{O_{hl}}(m_H)$ one can then obtain $O_{hl}(m_b)$ from the knowledge of $O_{hl}(m_c)$ provided that $\lambda^N = m_b/m_c$ for some integer N.

However, in the case of heavy quarkonia, the presence of different energy scales in (potential) NRQCD, and the fact that both charmonium and bottomonium systems may exhibit very distinct behavior relative to the one expected in the asymptotic limit, $m_H \to \infty$, implies that a simple scaling law valid from $m_H \simeq m_c, m_b$ up to $m_H \to \infty$ might not hold. For that reason, in this work we employ the ratio method only as a tool to reduce the statistical uncertainties and cutoff effects. After continuum extrapolation, we will determine the form factors employing Eq. (42) and discuss in the next Section the extrapolation of $F_1(m_H)$ to the physical point $m_H \to m_b$.

In order to reduce the UV cutoff effects induced by the local vector current of the heavy quark [$J_H^\mu(x)$], we find it useful to modify the estimator $\bar{r}_\lambda^{(n)}(t_h; t_J)$ as

$$\bar{r}_\lambda^{(n)}(t_h; t_J) \to \Delta_{\rm RC}^{(n)} \bar{r}_\lambda^{(n)}(t_h; t_J), \tag{44}$$

where

$$\Delta_{\rm RC}^{(n)} = \frac{Z_V^{\rm WI}(m_H^{(n)})}{Z_V^{\rm WI}(m_H^{(n-1)})} = 1 + O(a^2 m_H^2), \tag{45}$$

and where $Z_V^{\rm WI}(m_H)$ is the renormalization constant of the local vector current of the heavy quark, determined from the twisted-mass Ward identity as

$$Z_V^{\rm WI}(m_H) = \lim_{t \to \infty} 2 m_H \frac{\sum_{\mathbf{x}} \langle \mathcal{O}_{\eta_H}(\mathbf{x}, t) \bar{q}_H(0) \gamma^5 q'_H(0) \rangle}{\partial_t \sum_{\mathbf{x}} \langle \mathcal{O}_{\eta_H}(\mathbf{x}, t) \bar{q}_H(0) \gamma^5 \gamma^0 q'_H(0) \rangle}. \tag{46}$$

In Eq. (46), the primed field $q'_H(x)$ differs from the field $q_H(x)$ by the sign of the twisted Wilson term [see the discussion around Eq. (14)]. In Fig. 10, we show the estimators $\bar{r}_\lambda^{(n)}(t_h; t_J)$ for fixed $t_J \simeq 1.6$–1.7 fm, for $n = 2$, 3, 6 and for all gauge ensembles employed for the calculation. As the figure shows, like in the case of F_1^c, we find the cutoff effects to be remarkably small. The ratios $r_\lambda(m_H^{(n)})$ are always smaller than 1, about 0.9, and only smoothly dependent on n. Therefore, with increasing heavy quark mass the form factor $F_1(m_H)$ is decreasing, roughly by about 10% every after each increment of m_H by a factor of $\lambda = 1.24283$. Similarly to the case of $h_c \to \eta_c \gamma$, we carried out a study of the t_J dependence of our results by computing the three-point functions $C_{\rm 3pt}^\mu(t_h; t_J, m_H)$ on the B64 ensemble for a second value of $t_J \simeq 2.4$ fm. In Fig. 11 we show the comparison between the results obtained with $t_J \simeq 1.6$ fm and those obtained with $t_J \simeq 2.4$ fm for the ratios $r_\lambda(m_H^{(n)})$, with $n = 2$, 3, 4. As the figure shows, no differences are visible and, as in the case of $h_c \to \eta_c \gamma$, the

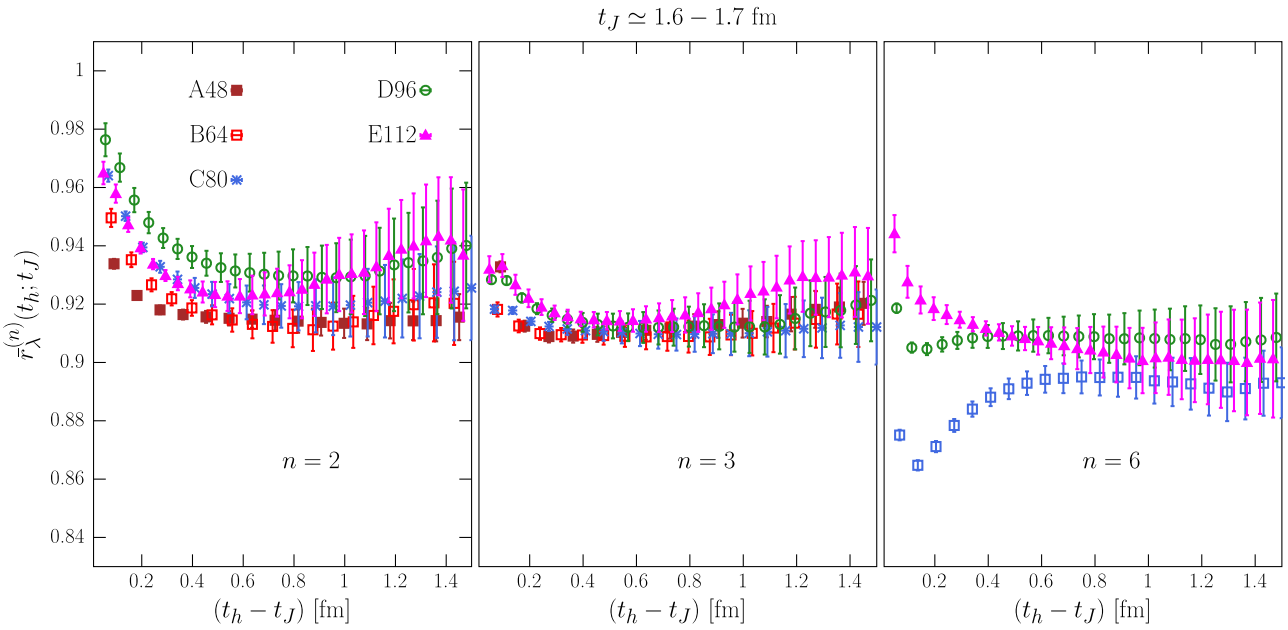

FIG. 10. The estimator $\bar{r}_\lambda^{(n)}(t_h; t_J)$ of the ratio $r_\lambda(m_H^{(n)})$ for $n = 2$ (left), $n = 3$ (middle) and $n = 6$ (right), for all the gauge ensembles used for the present computation, and for fixed $t_J \simeq 1.6$–1.7 fm. For $n = 2, 3$ results at five lattice spacings are available while for $n = 6$ the ratio is computed on three lattice spacings (C80, D96, E112).

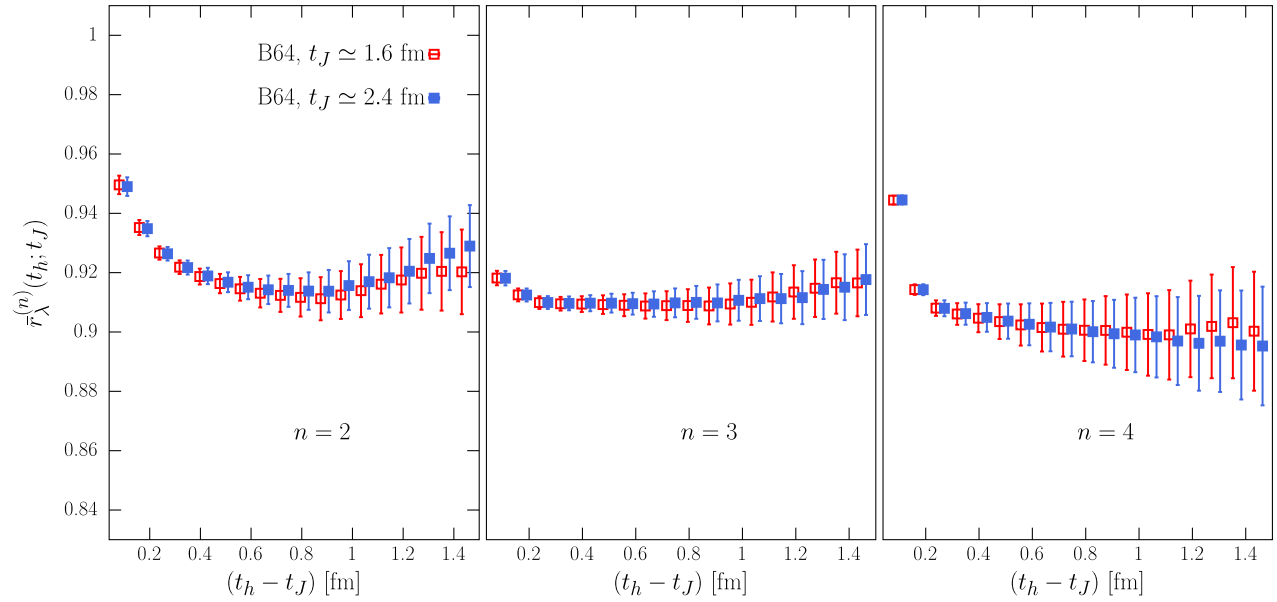

FIG. 11. Comparison between the results obtained for the estimators $r_\lambda^{(n)}(t_h; t_J)$ with $n = 2, 3, 4$ on the B64 ensemble for two different values of t_J, $t_J \simeq 1.6$ fm and $t_J \simeq 2.4$ fm.

statistical noise does not deteriorate while going for larger t_J, in line with expectations discussed in Sec. II A. On each gauge ensemble we extract the ratios $r_\lambda(m_H^{(n)})$ by fitting $\bar{r}_\lambda^{(n)}(t_h; t_J)$ to a constant in the region where a plateau is visible. Each of $r_\lambda(m_H^{(n)})$ now should be extrapolated to the continuum limit. Given the smallness of the UV cutoff effects in the ratios, we extrapolate our lattice data to the continuum limit through a simple linear fit in a^2, which is shown in Fig. 12. Contrary to the masses of η_H and h_H, where a^4 cutoff effects are clearly visible, in this case the lattice spacing dependence is very mild. The reduced χ^2 of the linear fits is always close to (or smaller than) unit. We also checked that the ratio method applied to the masses (m_{η_H} and m_{h_H}) gives results in the continuum limit fully

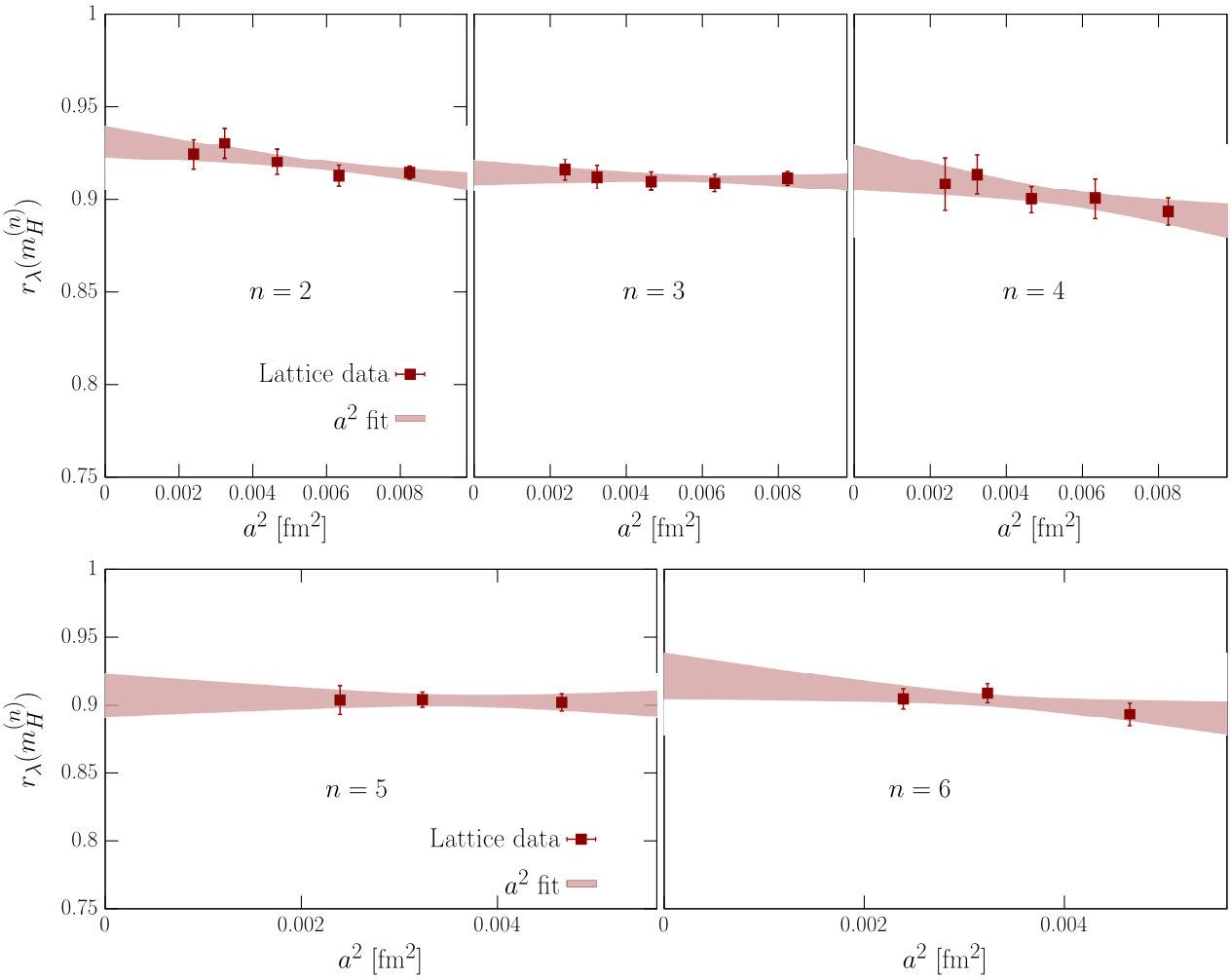

FIG. 12. Continuum-limit extrapolation for the ratios $r_\lambda(m_H^{(n)})$ with $n = 2$ (top-left), $n = 3$ (top-center), $n = 4$ (top-right), $n = 5$ (bottom-left) and $n = 6$ (bottom-right). The extrapolation is performed through a linear a^2 fit to the lattice data. In all cases we have $\chi^2/\text{dof} \lesssim 1$.

consistent with those we presented in III A. The last step of this analysis is the determination of the form factor $F_1(m_c)$. Whether we use $|\mathbf{k}|$ from the physical charmonia or bottomonia, the resulting $F_1(m_c)$ remains practically indistinguishable, as displayed in Fig. 13.[9] Finally, we obtain $F_1(m_H)$ by multiplying $F_1(m_c)$ and the ratios $r_\lambda(m_H^{(n)})$, cf. Eq. (42). The results are reported in Table V. We are now going to describe how to extrapolate the form factor to the physical b-quark mass.

C. Extrapolation $m_H \to m_b$

Electric-dipole induced transitions (E1) of heavy quarkonia, such as $h_b \to \eta_b\gamma$, have been studied in Ref. [49] using NRQCD [2,50], and in potential NRQCD (pNRQCD) [3,51,52]. In Ref. [49] it is found that the leading order expression for the decay rate $\Gamma(h_H \to \eta_H\gamma)$ as a function of the quark mass m_H reads[10]

$$\Gamma(h_H \to \eta_H\gamma) \propto \frac{|\mathbf{k}|^3}{(m_H)^2 v_H^2}[1 + O(m_H^{-1}, v_H^2)], \quad (47)$$

where the heavy quark velocity, $v_H \ll 1$, is a dynamical quantity, a function of the strong interaction scale Λ_{QCD}. In contrast to the heavy-light systems, in NRQCD the presence of different scales, Λ/m_H, v_H, …, and of their interplay, does not allow one to obtain a simple scaling relation.

For heavy quarkonia, two regimes are typically distinguished: the weakly coupled regime $m_H v_H^2 \gg \Lambda$, and the

[9]Obviously, $F_1(m_c)$ with $|\mathbf{k}|$ fixed by using the physical masses of charmonia coincides with F_1^c discussed in the previous Section.

[10]In NRQCD the heavy quark mass, appearing in Eq. (47), should be identified with the quark pole mass.

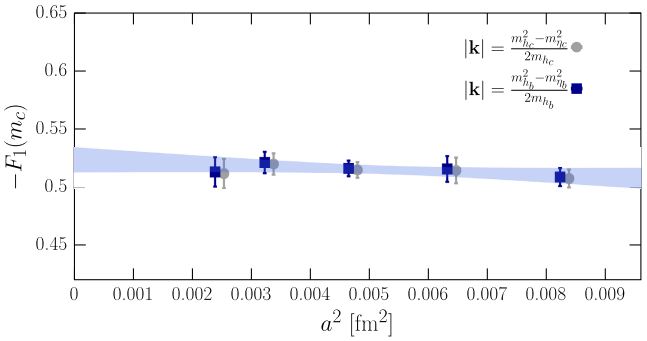

FIG. 13. Linear extrapolation of $F_1(m_c)$ in a^2 to the continuum limit (colored band). Data points obtained by fixing $|\mathbf{k}|$ by the physical masses of bottomonia (squares) are compared to those obtained in the previous section in which $|\mathbf{k}|$ was fixed by the physical masses of charmonia (circles) and slightly offset for easier comparison.

strongly coupled one $m_H v_H^2 \ll \Lambda$. The weakly coupled regime is approached in the asymptotic limit $m_H \to \infty$, in which the quark-antiquark system is mainly sensitive to the short distance Coulombic part of the quark-antiquark potential $V_H(r)$, given (up to higher-order corrections in α_s) by

$$V_H^{\text{pert}}(r) = -\frac{C_F \alpha_s(r)}{r}, \tag{48}$$

with $C_F = 4/3$ for QCD. In that situation, the following scaling law applies

$$\begin{aligned} v_H(m_H) &\propto \alpha_s(m_H v_H), \\ |k| \simeq \Delta m_{h\eta} &\propto m_H v_H^2 \propto m_H \alpha_s^2(m_H v_H), \end{aligned} \tag{49}$$

where $\Delta m_{h\eta} \equiv m_{h_H} - m_{\eta_H}$. From the comparison between Eq. (47) and Eq. (26), it follows that in the Coulombic limit the form factor $F_1(m_H)$ scales as $F_1(m_H) \propto \alpha_s(m_H v_H)$. Instead, in the strongly coupled regime the system is also sensitive to the long distance, nonperturbative, part of the quark-antiquark potential $V_H(r) \simeq \sigma r$.

Determining whether a given quarkonium state is weakly or strongly coupled is far from obvious. The ground states, such as $\eta_{c,b}$, are more likely to be weakly coupled: their wave functions are relatively localized around the system's center of mass and therefore they are likely to be more sensitive to the short distance part of the potential $V_H(r)$. In contrast, the excited states, such as $h_{c,b}$, tend to be more strongly coupled: their wave functions are more spread out and thus increasingly sensitive to the nonperturbative part of the potential.

In our case, we already noted that the photon momentum $-\mathbf{k}$ only slightly changes when going from m_c to m_b (by about 2%). Thus, considering $\mathbf{k}$ to be constant over the range $m_c \le m_H \le m_b$, the scaling relation in Eq. (47) corresponds to the following scaling relation for the form factor $F_1(m_H)$:

$$F_1(m_H) \propto \frac{|\mathbf{k}|}{m_H v_H}[1 + O(m_H^{-1}, v_H^2)]. \tag{50}$$

To extrapolate $F_1(m_H)$ to the physical b-quark mass, we adopt an agnostic approach. This is made possible by the fact that our data are sufficiently precise and span over a large enough range of heavy meson masses (with the heaviest simulated η_H being around 6.6 GeV). Therefore any reasonable *Ansatz* for the heavy mass dependence, that accurately describes the data in the simulated region, always yields results at the physical b-quark mass in the same ballpark. By performing a sufficiently large number of fits we can then properly determine the systematic error associated with the mass extrapolation.

We employ the following forms for the extrapolation of the form factor:

(i) Type A: We exploit the fact that $\Delta m_{h\eta}$ is roughly constant when going from m_c and m_b and that parametrically $\Delta m_{h\eta}$ is of the order $O(m_H v_H^2)$. We can therefore take $v_H \propto \sqrt{|\mathbf{k}|/m_H}$ so that from Eq. (50) we get that $F_1(m_H) \propto 1/\sqrt{m_H}$, up to $1/m_H$ corrections. Instead of the heavy quark mass one can use $m_{\eta_H}/2$, which is equivalent, up to higher order corrections in the velocity v_H. We can therefore use the form,

$$F_1(m_H)\sqrt{m_{\eta_H}} = \alpha + \frac{\beta}{m_{\eta_H}} + \frac{\gamma}{m_{\eta_H}^2}, \tag{51}$$

where α, β and γ are the fit parameters, independent on the heavy quark mass. In Fig. 14 we show that the scaling (51) is remarkably well verified by our lattice results. From the fit of our data to Eq. (51), either by

TABLE V. Values of the form factor $F_1(m_H^{(n)})$ and of the ratio $r_\lambda(m_H^{(n)})$ for each simulated value of the heavy-quark mass $m_H^{(n)} = \lambda^{n-1} m_c$, with $\lambda = 1.24283$.

	$m_H^{(1)}$	$m_H^{(2)}$	$m_H^{(3)}$	$m_H^{(4)}$	$m_H^{(5)}$	$m_H^{(6)}$
$-F_1(m_H^{(n)})$	0.523(10)	0.4872(91)	0.4455(83)	0.4086(89)	0.371(10)	0.342(13)
$r_\lambda(m_H^{(n)})$		0.9311(81)	0.9144(64)	0.917(12)	0.907(16)	0.921(17)

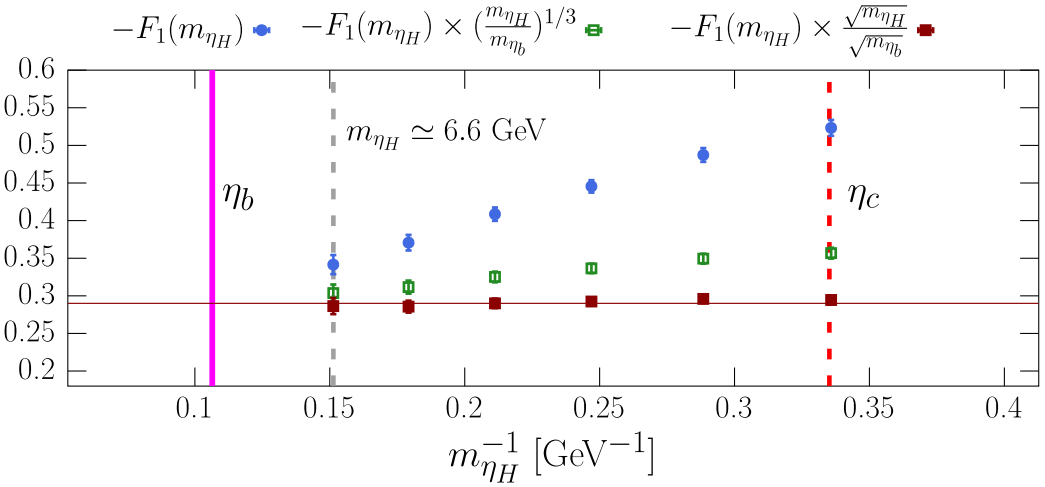

FIG. 14. In the figure we show our results for the form factor $F_1(m_{\eta_H})$ (blue circles) and for the combinations $F_1(m_H) \times (m_{\eta_H}/m_{\eta_b})^{1/3}$ (green empty squares) and $F_1(m_H) \times \sqrt{m_{\eta_H}}/\sqrt{m_{\eta_b}}$ (red filled squares). The horizontal line is added to guide the eye.

setting $\tilde{\beta} = \tilde{\gamma} = 0$, or by keeping them in the fit, we obtain

$$\text{TypeA: } F_1(m_b) \equiv F_1^b = -0.285(10). \quad (52)$$

(ii) Type B: If the static limit is dominated by the Coulombic potential, as discussed above, one has $v_H \propto \alpha_s(\frac{1}{2} m_{\eta_H} v_H)$ [49,52], and by combining Eqs. (49) with (50) we arrive at the fit form

$$F_1(m_H) = \alpha' + \frac{\beta'}{m_{\eta_H}} + \frac{\gamma'}{m_{\eta_H}^2}, \quad (53)$$

where again, α', β' and γ' are the heavy quark mass independent fit parameters. To us these are merely fit parameters, while in pNRQCD the authors compute the α' term by subtracting renormalon and using perturbative QCD to higher orders [52]. It is worth mentioning that from the linear fit to our data in $1/m_{\eta_H}$, we obtain $\alpha'_{\text{lin}} = -0.20(2)$ [$\gamma' = 0$ in Eq. (53)], while from the quadratic one we get $\alpha'_{\text{quad}} = -0.17(6)$, where in both cases we removed our lightest heavy quark from the fit. Again, by using the fit form (53), either by setting $\beta' = \gamma' = 0$, or by keeping them as free (fit parameters), we find

$$\text{TypeB: } F_1^b = -0.298(20). \quad (54)$$

(iii) Type C: If instead of the Coulombic potential we assume a purely string potential $V_H(r) = \sigma r$, we get that $v_H \propto m_{\eta_H}^{-2/3}$, which then together with Eq. (50) lead to our third heavy quark mass dependence,

$$F_1(m_H) m_{\eta_H}^{1/3} = \bar{\alpha} + \frac{\bar{\beta}}{m_{\eta_H}} + \frac{\bar{\gamma}}{m_{\eta_H}^2}. \quad (55)$$

After proceeding like in the previous two cases, we get

$$\text{TypeC: } F_1^b = -0.293(15). \quad (56)$$

In Fig. 14 we show the data and illustrate the quality of the scalings (51) and (53), to emphasize the amount of corrections $\propto 1/m_{\eta_H}$ and higher.

We fit our data using Eqs. (51), (53), (55) and for each type of fit we perform four different extrapolations: we first set the power corrections to zero and then include either the linear ($\propto 1/m_{\eta_H}$) or the quadratic term ($\propto 1/m_{\eta_H}^2$), and finally we include both of them. We also perform the fits by imposing cuts on the data which means that we repeated each of the above fits by excluding the data point corresponding to the lightest simulated $m_H = m_c$, and even by dropping the results corresponding to the lightest two of our heavy quarks. All fits have been performed by minimizing χ^2 that fully takes into account the cross correlations among the data. All these fit results are then combined using the BAIC, which has been already discussed in Sec. II B. In Fig. 15 we show the results of these extrapolations. The dashed lines correspond to the (central value of the) best fit curves, obtained in all the fits we performed (excluding those leading to $\chi^2/\text{dof} > 2$). In Fig. 15 we also show the final result obtained using the BAIC, namely,

$$\boxed{F_1^b = -0.290(15),} \quad (57)$$

which has an uncertainty of about 5%, three times larger than in the case of charmonia (24). Note that this is the first lattice QCD result of this quantity.

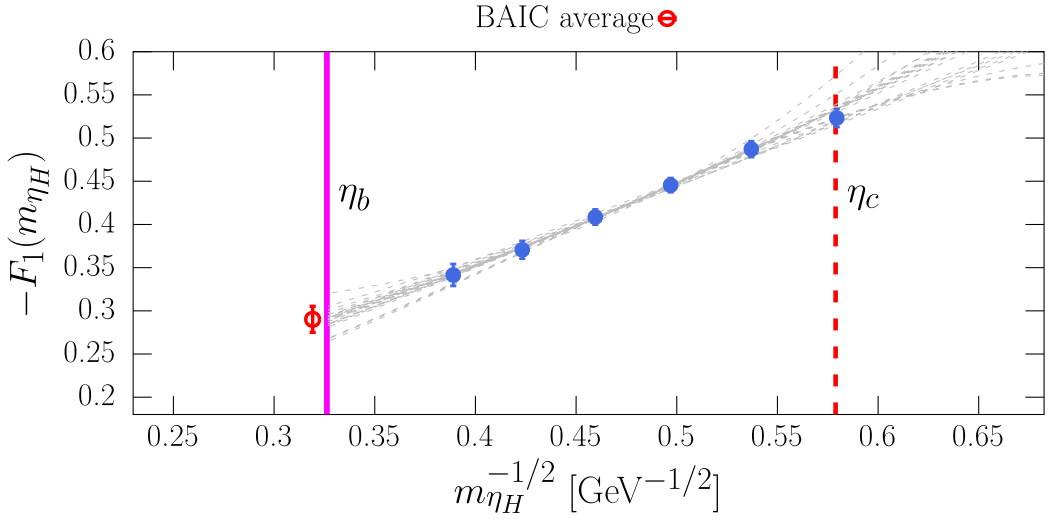

FIG. 15. Extrapolation of the form factor $F_1(m_H)$ to $F_1(m_b)$. Each of the black dashed curves corresponds to the best fit obtained in all of the fits we performed and discussed in the text. The red circle corresponds to the BAIC average of all fits, our final result. Since our results very well verify the scaling (51), we plot them as a function of $1/\sqrt{m_{\eta_H}}$.

IV. COMPARISON WITH EXISTING THEORETICAL AND EXPERIMENTAL RESULTS

In this Section we provide the decay widths $\Gamma(h_{c(b)} \to \eta_{c(b)}\gamma)$ and compare our results with existing experimental data and other lattice and nonlattice predictions.

Using the expression of Eq. (3) and our result for $F_1^c = -0.522(10)$, we obtain

$$\Gamma(h_c \to \eta_c\gamma) = (0.604 \pm 0.024)\ \text{MeV}, \tag{58}$$

where we used $\alpha_{\text{em}}^{-1}(m_c) = 133.5(5)$ [9]. Our result agrees with the experimental measurement by the BES-III Collaboration [53,54],

$$\Gamma(h_c \to \eta_c\gamma)^{\text{exp}} = (0.47 \pm 0.17)\ \text{MeV}, \tag{59}$$

although the current experimental uncertainty is much larger compared to ours. Note, however, that the experimental error is dominated by the total width, $\Gamma(h_c)^{\text{exp}} = (0.78 \pm 0.28)$ MeV [9], which is about 35%, while the uncertainty on the branching fraction is relatively small (7%). We can therefore combine our lattice QCD result (58) with $\mathcal{B}(h_c \to \eta_c\gamma)^{\text{exp}} = (60 \pm 4)\%$ [9] and estimate $\Gamma(h_c)$. We obtain

$$\Gamma(h_c)^{\text{latt+exp}} = \frac{\Gamma(h_c \to \eta_c\gamma)^{\text{latt}}}{\mathcal{B}(h_c \to \eta_c\gamma)^{\text{exp}}} = (1.007 \pm 0.078)\ \text{MeV}. \tag{60}$$

This result has more than four times smaller error that the experimentally measured total width [54].

Our $F_1^c = -0.522(10)$ is a substantial improvement over $F_1^c = -0.57(2)(1)$ of Ref. [30] because it is obtained with $N_f = 2+1+1$ dynamical quark flavors and (more importantly) with the physical sea quark masses. Their rate, $\Gamma(h_c \to \eta_c\gamma) = 0.72(5)(2)$ MeV, is about 2σ larger than our result (58).[11] To the best of our knowledge there are only two other lattice QCD results. On the basis of a quenched lattice calculation, the rate $\Gamma(h_c \to \eta_c\gamma) = 0.601(55)$ MeV has been reported in Ref. [29], in agreement with our result (58). In Ref. [55], instead, by using $N_f = 2$ twisted-mass fermions at a single lattice spacing ($a \simeq 0.07$ fm) the authors quote $\Gamma(h_c \to \eta_c\gamma) = 0.234(12)$ MeV, much smaller than our result. In Fig. 16 we show a comparison of different lattice results with the existing model and experimental determinations of the radiative decay rate.

We now discuss $h_b \to \eta_b\gamma$. Like in the case of charmonia, we insert our result $F_1^b = -0.290(15)$, in the expression of Eq. (26) and obtain

$$\Gamma(h_b \to \eta_b\gamma) = (46.0 \pm 4.8)\ \text{keV}, \tag{61}$$

where we used $\alpha_{\text{em}}^{-1}(m_b) = 132.2(3)$ [9]. Our result for the decay rate thus has an uncertainty of about 10%. In this case only the branching fraction has been measured $\mathcal{B}(h_b \to \eta_b\gamma)^{\text{exp}} = 52^{+6}_{-5}\%$ [9,19,20]. We can combine that result with our decay width estimate (61) and predict the total width of h_b. We get,

$$\Gamma(h_b)^{\text{latt+exp}} = \frac{\Gamma(h_b \to \eta_b\gamma)^{\text{latt}}}{\mathcal{B}(h_b \to \eta_b\gamma)^{\text{exp}}} = (88 \pm 13)\ \text{keV}. \tag{62}$$

[11]Note that we corrected the expression for the matrix element in Ref. [30].

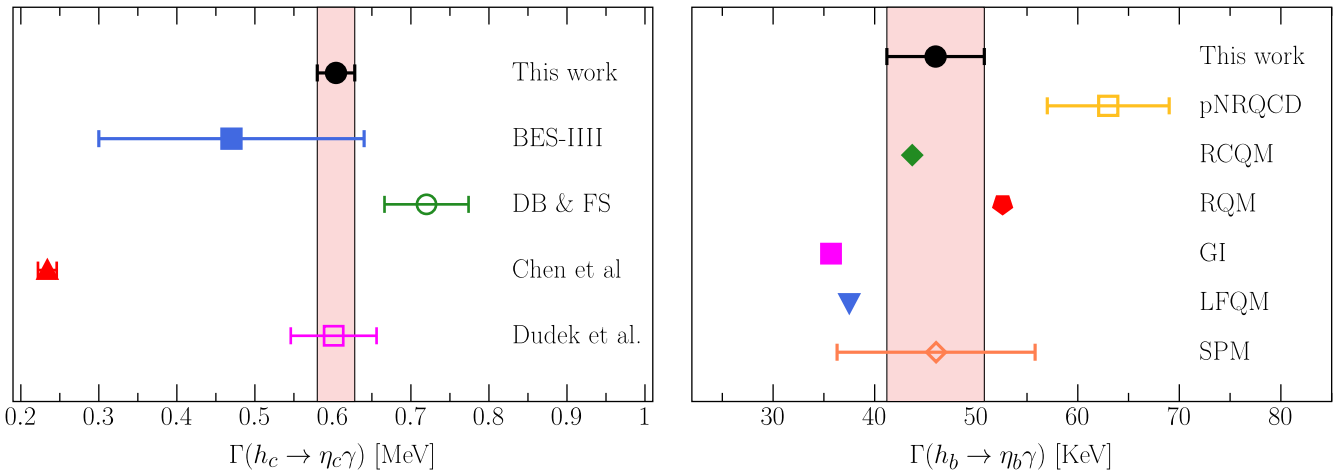

FIG. 16. Comparison of our estimate of the radiative decay widths $\Gamma(h_{c,b} \to \eta_{c,b}\gamma)$ (filled black circle) with results available in the literature. In the case of charm we compare with the BES-III measurement [53,54] (filled blue square), and the previous lattice results: Ref. [30] (empty green circle), [55] (filled red triangle), and [29] (empty magenta square). In the right panel we compare our result for the bottomonium with other approaches [labels with corresponding references can be found in the text, after Eq. (62)].

Since no other lattice QCD result relevant to $h_b \to \eta_b\gamma$ is available, we compare our estimate for the decay width (61) with the value obtained by using potential NRQCD [52] and labeled as pNRQCD in Fig. 16. We also compare our result with various (relativistic) quark models which are labeled in Fig. 16 as RCQM [56], RQM [57], GI [58], LFQM [59], and SPM [60]. The overall agreement is good; the largest differences are with Ref. [58], which is 2σ below our result, and with the determination obtained using pNRQCD at weak coupling, which is a little over 2σ larger than our result.

V. CONCLUSIONS

In this paper we provide the full QCD computation of the form factors relevant to the radiative decays $h_{c,b} \to \eta_{c,b}\gamma$.

The result for the charmonium case is $F_1^c = -0.522(10)$ and is a very significant improvement over the previous lattice determinations because it is obtained with the physical sea quark masses with $N_f = 2 + 1 + 1$ and with five fine lattices, allowing a smooth extrapolation to the continuum limit. For the reasons explained in the text, we dropped the disconnected diagrams in this calculation. Their impact can and should be studied separately. We plan to do so using the Hansen-Lupo-Tantalo method of Ref. [61] to overcome the difficulties of isolating the charmonium and bottomonium contributions in the quark-disconnected terms. Our final result for the corresponding decay width is $\Gamma(h_c \to \eta_c\gamma) = (0.604 \pm 0.024)$ MeV.

We produced the first lattice QCD estimate of the form factor relevant to $h_b \to \eta_b\gamma$. Our result $F_1^b = -0.290(15)$ is obtained through a heavy quark extrapolation of the results obtained by working with the charm quark and a series of quarks heavier than charm, up to three times the charm quark mass. After a controlled extrapolation to the continuum limit, we made extrapolation from the fictitious F_1^H and m_{η_H} to the desired (physical) F_1^b and η_b. To do so we considered several options and performed many different fits. It should be emphasized that our results exhibit a very pronounced scaling of $F_1^H\sqrt{m_{\eta_H}} =$ constant, an observation that might be useful for pNRQCD studies. Like in the case of charmonia, also in this case we dropped the disconnected diagrams assuming their contribution to be negligibly small. From our estimate of the form factor F_1^b, we obtain $\Gamma(h_b \to \eta_b\gamma) = (46.0 \pm 4.8)$ keV, which is also the first lattice QCD based determination of this quantity.

The open-source packages tmLQCD[62–65], LEMON [66], DD-αAMG [67–70], QPHIX [71,72] and QUDA [73–75] have been used in the ensemble generation.

ACKNOWLEDGMENTS

We thank the ETMC for the most enjoyable collaboration, N. Brambilla and A. Vairo for helpful communication regarding the extrapolation of the form factor to the b-quark mass, and S. Simula for useful discussions. V. L., F. S., G. G., R. F., and N. T. are supported by the Italian Ministry of University and Research (MUR) and the European Union (EU)—Next Generation EU, Mission 4, Component 1, PRIN 2022, CUP F53D23001480006. F. S. is supported by Italian Research Center on High Performance Computing, Big Data and Quantum Computing (ICSC)—Centro Nazionale di Ricerca in High Performance Computing, Big Data and Quantum Computing, funded by European Union—Next Generation EU and by Italian Ministry of University and Research (MUR) projects FIS_00001556 and PRIN_2022N4W8WR. We acknowledge support from the LQCD123, ENP, and SPIF Scientific Initiatives of the Italian Nuclear Physics Institute (INFN). This project has received support from the European

Union's Horizon 2020 research and innovation program under the Marie Sklodowska-Curie Grant Agreements No. 860881-HIDDeN and No. 101086085-ASYMMETRY and the IN2P3 (CNRS) Master Project HighPTflavor. We gratefully acknowledge the ICSC—Centro Nazionale di Ricerca in High Performance Computing for providing computing time under the allocations RAC 1916318. We gratefully acknowledge CINECA for the provision of GPU time on Leonardo supercomputing facilities under the specific initiative INFN-LQCD123, and under Project No. IscrB VITO-QCD and Project No. IscrB SemBD. We gratefully acknowledge EuroHPC Joint Undertaking for awarding us access to MareNostrum5 through the Project No. EHPC-EXT-2024E01-031. The authors gratefully acknowledge the Gauss Centre for Supercomputing e.V. for funding this project by providing computing time on the GCS Supercomputers SuperMUC-NG at Leibniz Supercomputing Centre. The authors acknowledge the Texas Advanced Computing Center (TACC) at The University of Texas at Austin for providing HPC resources (Project No. PHY21001). We gratefully acknowledge PRACE for awarding access to HAWK at HLRS within the project with Id Acid 4886. We acknowledge the Swiss National Supercomputing Centre (CSCS) and the EuroHPC Joint Undertaking for awarding this project access to the LUMI supercomputer, owned by the EuroHPC Joint Undertaking, hosted by CSC (Finland) and the LUMI consortium through the Chronos programme under Project No. CH17-CSCS-CYP. We acknowledge EuroHPC Joint Undertaking for awarding the Project No. EHPC-EXT-2023E02-052 access to MareNostrum5 hosted by at the Barcelona Supercomputing Center, Spain.

DATA AVAILABILITY

The data that support the findings of this article are not publicly available upon publication because it is not technically feasible and/or the cost of preparing, depositing, and hosting the data would be prohibitive within the terms of this research project. The data are available from the authors upon reasonable request.

[1] B. Aubert *et al.* (*BABAR* Collaboration), Phys. Rev. Lett. **101**, 071801 (2008); **102**, 029901(E) (2009).
[2] G. T. Bodwin, E. Braaten, and G. P. Lepage, Phys. Rev. D **51**, 1125 (1995); **55**, 5853(E) (1997).
[3] N. Brambilla, A. Pineda, J. Soto, and A. Vairo, Nucl. Phys. **B566**, 275 (2000).
[4] S. Fleming, I. Z. Rothstein, and A. K. Leibovich, Phys. Rev. D **64**, 036002 (2001).
[5] N. Brambilla, A. Pineda, J. Soto, and A. Vairo, Rev. Mod. Phys. **77**, 1423 (2005).
[6] B. G. Fulsom *et al.* (Belle Collaboration), Phys. Rev. Lett. **121**, 232001 (2018).
[7] G. Bonvicini *et al.* (CLEO Collaboration), Phys. Rev. D **81**, 031104 (2010).
[8] B. Aubert *et al.* (*BABAR* Collaboration), Phys. Rev. Lett. **103**, 161801 (2009).
[9] S. Navas *et al.* (Particle Data Group), Phys. Rev. D **110**, 030001 (2024).
[10] A. G. Shamov and O. L. Rezanova, Phys. Lett. B **839**, 137766 (2023).
[11] B. A. Kniehl, A. A. Penin, A. Pineda, V. A. Smirnov, and M. Steinhauser, Phys. Rev. Lett. **92**, 242001 (2004); **104**, 199901(E) (2010).
[12] S. Recksiegel and Y. Sumino, Phys. Lett. B **578**, 369 (2004).
[13] T. Manke *et al.* (*CP*-PACS Collaboration), Phys. Rev. D **62**, 114508 (2000).
[14] X. Liao and T. Manke, Phys. Rev. D **65**, 074508 (2002).
[15] A. X. El-Khadra, A. S. Kronfeld, and P. B. Mackenzie, Phys. Rev. D **55**, 3933 (1997).
[16] T. Burch, C. DeTar, M. Di Pierro, A. X. El-Khadra, E. D. Freeland, S. Gottlieb, A. S. Kronfeld, L. Levkova, P. B. Mackenzie, and J. N. Simone, Phys. Rev. D **81**, 034508 (2010).
[17] S. Meinel, Phys. Rev. D **82**, 114502 (2010).
[18] R. J. Dowdall *et al.* (HPQCD Collaboration), Phys. Rev. D **85**, 054509 (2012).
[19] U. Tamponi *et al.* (Belle Collaboration), Phys. Rev. Lett. **115**, 142001 (2015).
[20] R. Mizuk *et al.* (Belle Collaboration), Phys. Rev. Lett. **109**, 232002 (2012).
[21] S. Andreas, O. Lebedev, S. Ramos-Sanchez, and A. Ringwald, J. High Energy Phys. 08 (2010) 003.
[22] R. Dermisek and J. F. Gunion, Phys. Rev. D **81**, 075003 (2010).
[23] F. Domingo, U. Ellwanger, and M.-A. Sanchis-Lozano, Phys. Rev. Lett. **103**, 111802 (2009).
[24] R. Dermisek, J. F. Gunion, and B. McElrath, Phys. Rev. D **76**, 051105 (2007).
[25] J. E. Kim, Phys. Rep. **150**, 1 (1987).
[26] L. Merlo, F. Pobbe, S. Rigolin, and O. Sumensari, J. High Energy Phys. 06 (2019) 091.
[27] M. Bauer, M. Neubert, S. Renner, M. Schnubel, and A. Thamm, J. High Energy Phys. 09 (2022) 056.
[28] L. Di Luzio, A. W. M. Guerrera, X. Ponce Díaz, and S. Rigolin, J. High Energy Phys. 06 (2024) 217.
[29] J. J. Dudek, R. G. Edwards, and D. G. Richards, Phys. Rev. D **73**, 074507 (2006).
[30] D. Becirevic and F. Sanfilippo, J. High Energy Phys. 01 (2013) 028.
[31] G. C. Donald, C. T. H. Davies, E. Follana, K. Hornbostel, J. Komijani, J. Koponen, G. P. Lepage, C. McNeile, and J. Shigemitsu, Phys. Rev. D **86**, 094501 (2012).

[32] B. Colquhoun, L. J. Cooper, C. T. H. Davies, and G. P. Lepage (Particle Data Group, HPQCD Collaborations), Phys. Rev. D **108**, 014513 (2023).
[33] B. Blossier *et al.* (ETM Collaboration), J. High Energy Phys. 04 (2010) 049.
[34] R. Frezzotti and G. C. Rossi, J. High Energy Phys. 08 (2004) 007.
[35] R. Frezzotti and G. C. Rossi, J. High Energy Phys. 10 (2004) 070.
[36] C. Alexandrou *et al.* (Extended Twisted Mass Collaboration (ETMC)), Phys. Rev. D **111**, 054502 (2025).
[37] B. Sheikholeslami and R. Wohlert, Nucl. Phys. **B259**, 572 (1985).
[38] R. Di Palma, G. Gagliardi, and F. Sanfilippo, Proc. Sci., LATTICE2023 (**2024**) 152.
[39] D. Hatton, C. T. H. Davies, B. Galloway, J. Koponen, G. P. Lepage, and A. T. Lytle (HPQCD Collaboration), Phys. Rev. D **102**, 054511 (2020).
[40] R. G. Petry, D. Harnett, R. Lewis, and R. M. Woloshyn, Phys. Rev. D **78**, 074502 (2008).
[41] E. T. Neil and J. W. Sitison, Phys. Rev. D **109**, 014510 (2024).
[42] Y. Aoki *et al.*, FLAG review 2024, arXiv:2411.04268.
[43] P. Dimopoulos *et al.* (ETM Collaboration), J. High Energy Phys. 01 (2012) 046.
[44] A. Bussone *et al.* (ETM Collaboration), Phys. Rev. D **93**, 114505 (2016).
[45] N. Carrasco *et al.* (ETM Collaboration), J. High Energy Phys. 03 (2014) 016.
[46] R. Balasubramamian and B. Blossier, Eur. Phys. J. C **80**, 412 (2020).
[47] M. Atoui, V. Morénas, D. Bečirevic, and F. Sanfilippo, Eur. Phys. J. C **74**, 2861 (2014).
[48] B. Blossier, P.-H. Cahue, J. Heitger, S. La Cesa, J. Neuendorf, and S. Zafeiropoulos, Phys. Rev. D **105**, 054515 (2022).
[49] N. Brambilla, P. Pietrulewicz, and A. Vairo, Phys. Rev. D **85**, 094005 (2012).
[50] W. E. Caswell and G. P. Lepage, Phys. Lett. B **167**, 437 (1986).
[51] A. Pineda and J. Soto, Nucl. Phys. B, Proc. Suppl. **64**, 428 (1998).
[52] J. Segovia, S. Steinbeißer, and A. Vairo, Phys. Rev. D **99**, 074011 (2019).
[53] M. Ablikim *et al.* (BESIII Collaboration), Phys. Rev. Lett. **116**, 251802 (2016).
[54] M. Ablikim *et al.* (BESIII Collaboration), Phys. Rev. D **106**, 072007 (2022).
[55] Y. Chen *et al.*, Phys. Rev. D **84**, 034503 (2011).
[56] J. Segovia, P. G. Ortega, D. R. Entem, and F. Fernández, Phys. Rev. D **93**, 074027 (2016).
[57] D. Ebert, R. N. Faustov, and V. O. Galkin, Phys. Rev. D **67**, 014027 (2003).
[58] S. Godfrey and K. Moats, Phys. Rev. D **92**, 054034 (2015).
[59] Y.-L. Shi, Eur. Phys. J. C **77**, 253 (2017).
[60] B.-Q. Li and K.-T. Chao, Commun. Theor. Phys. **52**, 653 (2009).
[61] M. Hansen, A. Lupo, and N. Tantalo, Phys. Rev. D **99**, 094508 (2019).
[62] K. Jansen and C. Urbach, Comput. Phys. Commun. **180**, 2717 (2009).
[63] A. Abdel-Rehim, F. Burger, A. Deuzeman, K. Jansen, B. Kostrzewa, L. Scorzato, and C. Urbach, Proc. Sci., LATTICE2013 (**2014**) 414 [arXiv:1311.5495].
[64] A. Deuzeman, K. Jansen, B. Kostrzewa, and C. Urbach, Proc. Sci., LATTICE2013 (**2014**) 416 [arXiv:1311.4521].
[65] B. Kostrzewa, S. Bacchio, J. Finkenrath, M. Garofalo, F. Pittler, S. Romiti, and C. Urbach (ETM Collaboration), Proc. Sci., LATTICE2022 (**2023**) 340 [arXiv:2212.06635].
[66] A. Deuzeman, S. Reker, and C. Urbach (ETM Collaboration), Comput. Phys. Commun. **183**, 1321 (2012).
[67] A. Frommer, K. Kahl, S. Krieg, B. Leder, and M. Rottmann, SIAM J. Sci. Comput. **36**, A1581 (2014).
[68] C. Alexandrou, S. Bacchio, J. Finkenrath, A. Frommer, K. Kahl, and M. Rottmann, Phys. Rev. D **94**, 114509 (2016).
[69] S. Bacchio, C. Alexandrou, and J. Finkerath, EPJ Web Conf. **175**, 02002 (2018).
[70] C. Alexandrou, S. Bacchio, and J. Finkenrath, Comput. Phys. Commun. **236**, 51 (2019).
[71] B. Joó, D. D. Kalamkar, T. Kurth, K. Vaidyanathan, and A. Walden, in *High Performance Computing: ISC High Performance 2016 International Workshops, ExaComm, E-MuCoCoS, HPC-IODC, IXPUG, IWOPH, P^ 3 MA, VHPC, WOPSSS, Frankfurt, Germany, 2016, Revised Selected Papers 31* (Springer, New York, 2016), pp. 415–427.
[72] M. Schröck, S. Simula, and A. Strelchenko, Proc. Sci., LATTICE2015 (**2016**) 030 [arXiv:1510.08879].
[73] M. A. Clark, R. Babich, K. Barros, R. C. Brower, and C. Rebbi, Comput. Phys. Commun. **181**, 1517 (2010).
[74] R. Babich, M. A. Clark, B. Joo, G. Shi, R. C. Brower, and S. Gottlieb, in *SC11 International Conference for High Performance Computing, Networking, Storage and Analysis Seattle, Washington, 2011* (2011), arXiv:1109.2935.
[75] M. A. Clark, B. Joó, A. Strelchenko, M. Cheng, A. Gambhir, and R. C. Brower, in *SC '16: Proceedings of the International Conference for High Performance Computing, Networking, Storage and Analysis* (2016), pp. 795–806, arXiv:1612.07873.